Yeast Ataxin-2 Forms an Intracellular Condensate Required for the Inhibition of TORC1 Signaling during Respiratory Growth

Yang, Yu-San; Kato, Masato; Wu, Xi; Litsios, Athanasios; Sutter, Benjamin M; Wang, Yun; Hsu, Chien-Hsiang; Wood, N Ezgi; Lemoff, Andrew; Mirzaei, Hamid

Published in:
Cell

DOI:
10.1016/j.cell.2019.02.043

Article

Cell

Yeast Ataxin-2 Forms an Intracellular Condensate Required for the Inhibition of TORC1 Signaling during Respiratory Growth

Graphical Abstract

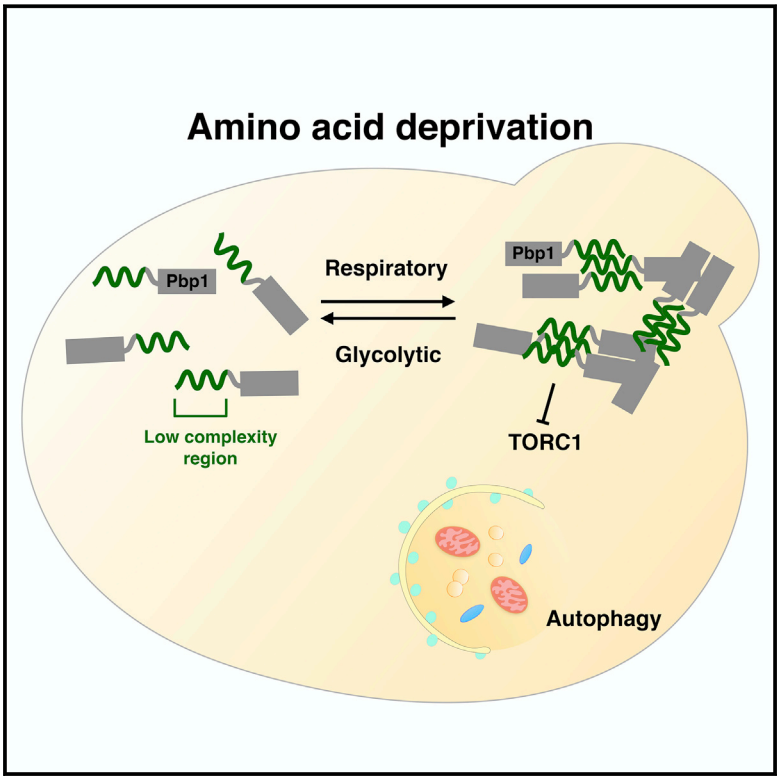

Authors

Yu-San Yang, Masato Kato, Xi Wu, ..., Hamid Mirzaei, Matthias Heinemann, Benjamin P. Tu

Correspondence

benjamin.tu@utsouthwestern.edu

In Brief

Unpacking the role of yeast ataxin-2 reveals that it preserves mitochondrial homeostasis, undergoing a condition-sensitive phase transition to modulate TORC1 function.

Highlights

- Pbp1 is a negative regulator of TORC1 required during respiratory growth
- A methionine-rich low complexity region of Pbp1 mediates formation of a condensate
- Mutations that weaken phase separation *in vitro* compromise TORC1 inhibition *in vivo*
- Loss of Pbp1 function leads to mitochondrial dysfunction and reduced survivability

Yang et al., 2019, Cell *177*, 697–710
April 18, 2019
https://doi.org/10.1016/j.cell.2019.02.043

CellPress

Article

Cell

Yeast Ataxin-2 Forms an Intracellular Condensate Required for the Inhibition of TORC1 Signaling during Respiratory Growth

Yu-San Yang,[1] Masato Kato,[1] Xi Wu,[1] Athanasios Litsios,[2] Benjamin M. Sutter,[1] Yun Wang,[1] Chien-Hsiang Hsu,[3,4] N. Ezgi Wood,[5] Andrew Lemoff,[1] Hamid Mirzaei,[1] Matthias Heinemann,[2] and Benjamin P. Tu[1,6,*]

[1]Department of Biochemistry, University of Texas Southwestern Medical Center, Dallas, TX 75390, USA

[2]Molecular Systems Biology, Groningen Biomolecular Sciences and Biotechnology Institute, University of Groningen, Groningen 9747AG, the Netherlands

[3]Simmons Cancer Center, University of Texas Southwestern Medical Center, Dallas, TX 75390, USA

[4]Department of Pharmaceutical Chemistry, University of California, San Francisco, San Francisco, CA 94158, USA

[5]Department of Cell Biology, University of Texas Southwestern Medical Center, Dallas, TX 75390, USA

[6]Lead Contact

*Correspondence: benjamin.tu@utsouthwestern.edu

https://doi.org/10.1016/j.cell.2019.02.043

SUMMARY

Yeast ataxin-2, also known as Pbp1 (polyA binding protein-binding protein 1), is an intrinsically disordered protein implicated in stress granule formation, RNA biology, and neurodegenerative disease. To understand the endogenous function of this protein, we identify Pbp1 as a dedicated regulator of TORC1 signaling and autophagy under conditions that require mitochondrial respiration. Pbp1 binds to TORC1 specifically during respiratory growth, but utilizes an additional methionine-rich, low complexity (LC) region to inhibit TORC1. This LC region causes phase separation, forms reversible fibrils, and enables self-association into assemblies required for TORC1 inhibition. Mutants that weaken phase separation *in vitro* exhibit reduced capacity to inhibit TORC1 and induce autophagy. Loss of Pbp1 leads to mitochondrial dysfunction and reduced fitness during nutritional stress. Thus, Pbp1 forms a condensate in response to respiratory status to regulate TORC1 signaling.

INTRODUCTION

TORC1 is a protein kinase complex that regulates many cellular processes including protein translation and cellular metabolism in response to nutrient availability (Wullschleger et al., 2006). Inhibition of TORC1 leads to the induction of autophagy, a process that degrades cytoplasmic contents and organelles to maintain cell viability during nutrient starvation (Levine and Klionsky, 2004). Dysregulation of TORC1 signaling and inhibition of autophagy have been associated with cancer and neurodegenerative diseases (Boland et al., 2008; Nixon, 2013; Ravikumar et al., 2004). Precisely how cells sense their metabolic state to alternately regulate anabolic versus catabolic processes mediated by TORC1 has yet to be fully elucidated.

We previously reported that when prototrophic yeast cells are switched from a rich (YP) to a minimal (S) medium using a non-fermentable carbon source (lactate), they induce autophagy despite the presence of nitrogen (Wu and Tu, 2011). This autophagy-inducing regimen that forces cells to heavily utilize mitochondria enabled us to identify additional autophagy regulators that become essential outside of highly glycolytic growth conditions. Using a visual screen, we identified genes encoding a complex of three proteins (Iml1-Npr2-Npr3) specifically required for the induction of autophagy following the switch from YPL to SL medium, but not for autophagy triggered by the complete nitrogen starvation in high glucose (SD-N medium) (Wu and Tu, 2011). This complex has emerged as the more evolutionary conserved negative regulator of TORC1 that functions in response to amino acid insufficiency (Bar-Peled et al., 2013; Panchaud et al., 2013).

Since our first report of this screen, we have sequenced additional transposon mutants that are defective in autophagy following the switch from YPL to SL medium. Here, we show that Pbp1, the yeast ortholog of mammalian ataxin-2, is also a previously unrecognized regulator of autophagy. Pbp1 and ataxin-2 are intrinsically disordered proteins that had earlier been implicated in stress granule assembly and RNA biology (Buchan et al., 2008; Nonhoff et al., 2007; Ralser et al., 2005). Trinucleotide repeat expansions in ataxin-2 are strongly linked to neurodegenerative diseases such as spinocerebellar ataxia and amyotrophic lateral sclerosis (Alves-Cruzeiro et al., 2016; Elden et al., 2010). However, the normal endogenous function of Pbp1/ataxin-2 and the resulting impact of expanded glutamine tracts are not well understood. Here, we show how Pbp1 functions as a bona fide negative regulator of TORC1 signaling via an unconventional mechanism involving metabolic state-induced phase separation. Elucidation of this endogenous function for Pbp1 and its mechanism of action may provide useful insight into how mutant, polyglutamine-expanded forms are associated with increased risk of neurodegenerative conditions.

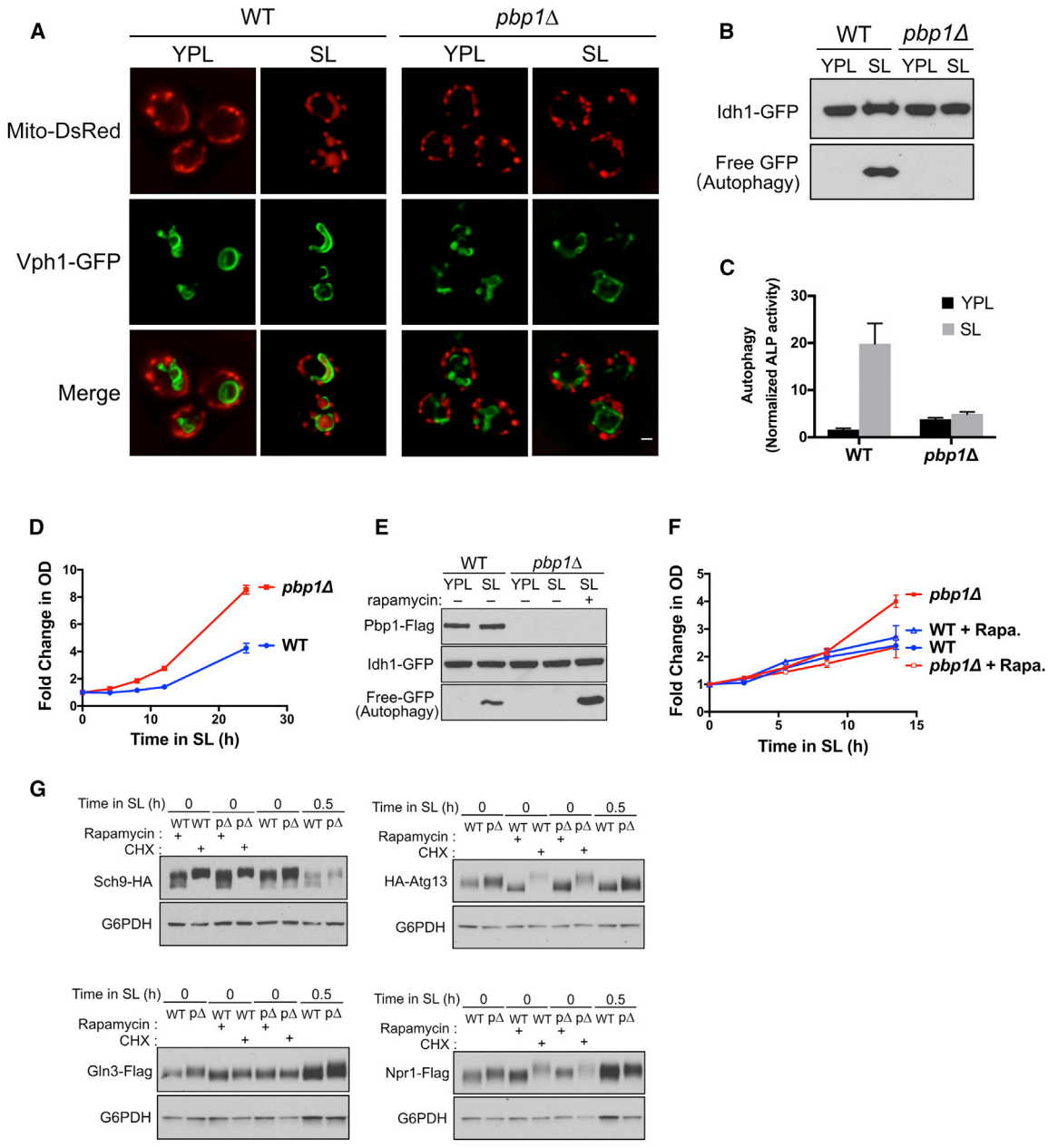

Figure 1. Pbp1 Induces Autophagy during Respiratory Growth by Inhibiting TORC1 Signaling

(A) Images of WT and *pbp1Δ* cells before and after switching from YPL to SL medium for 8 h. The accumulation of the mitochondria-targeted RFP (Mito-DsRed) reporter in the vacuole (Vph1-GFP) indicates mitophagy. *pbp1Δ* mutant cells were unable to induce mitophagy following switch to SL medium. Scale bar, 1 μm.

(B) GFP cleavage assay. The accumulation of free GFP following switch to SL medium indicates mitophagy. *pbp1Δ* cells were unable to induce mitophagy following switch to SL medium.

(C) ALP activity assay. Using a cytosolic alkaline phosphatase reporter, general autophagy was monitored using the alkaline phosphatase assay as described previously (Noda et al., 1995) and in STAR Methods. *pbp1Δ* cells were unable to induce general autophagy following switch to SL medium. Data were mean ± SD from 5 independent experiments.

(D) Growth of WT and *pbp1Δ* cells in SL medium. *pbp1Δ* cells exhibited increased cell growth in SL medium. Data were mean ± SD from 3 independent experiments.

(E) GFP cleavage assay reflecting autophagy amounts in *pbp1Δ* cells in SL medium with or without rapamycin (200 nM). Treatment with rapamycin completely restored autophagy in *pbp1Δ* cells.

(F) Growth of WT and *pbp1Δ* cells in SL medium containing 2 nM rapamycin. Treatment of rapamycin reversed the increased growth of *pbp1Δ* cells. Data were mean ± SD from 3 independent experiments. Rapa., rapamycin.

(legend continued on next page)

RESULTS

Pbp1 Regulates Autophagy and Cell Growth under Conditions that Require Mitochondrial Respiration

To interrogate a possible role for Pbp1 in the regulation of autophagy, we assayed autophagy in wild-type (WT) and *pbp1Δ* cells under a growth condition that requires mitochondrial respiration (Figures 1A–1C). In the presence of the non-fermentable carbon source lactate, cells lacking Pbp1 were unable to induce autophagy following the switch from rich (YPL) to minimal (SL) medium as determined by three different assays: appearance of Mito-DsRed reporter in vacuoles (Figure 1A), the GFP-cleavage assay that is indicative of mitophagy (Figure 1B), and the alkaline phosphatase (ALP) reporter assay as a quantitative measure of general autophagy (Figure 1C). In contrast, *pbp1Δ* mutants showed no deficit in autophagy induction upon switch to the more commonly utilized high glucose, nitrogen starvation condition (SD-N medium) (Figures S1A and S1B). These data suggest that the function of Pbp1 is selectively required when cell growth is restricted by non-fermentable carbon sources that require an increased dependency on mitochondria for energy.

Suppression of autophagy by deletion of core autophagy machinery components severely impedes cell growth following the switch to SL medium (Wu and Tu, 2011). Surprisingly, *pbp1Δ* cells exhibited a significantly increased growth rate in SL medium despite the lack of autophagy (Figure 1D), indicative of dysregulation of cellular growth control pathways. This increased growth phenotype of *pbp1Δ* was not observed when glucose was present as the carbon source (Figure S1C). Taken together, the lack of autophagy and abnormal growth phenotypes of *pbp1*Δ mutant cells in SL medium indicate the protein is involved in the regulation of cell growth under conditions that require mitochondrial respiration.

Pbp1 Functions by Negatively Regulating TORC1 Signaling

These phenotypes of *pbp1Δ* cells were reminiscent of mutants lacking the function of a three-protein complex (Iml1-Npr2-Npr3) previously identified to be required for autophagy under these conditions (Sutter et al., 2013; Wu and Tu, 2011). Subsequent work revealed that this complex, termed SEACIT or GATOR1, acts as a negative regulator of TORC1 (Bar-Peled et al., 2013; Panchaud et al., 2013). Interestingly, *iml1Δ*, *npr2Δ*, and *npr3Δ* mutants all bypass autophagy and exhibit an increased growth rate in SL medium (Laxman et al., 2013; Wu and Tu, 2011), just like *pbp1Δ* mutants. These similarities suggest that the autophagy and growth phenotypes of *pbp1Δ* mutants might also be due to hyperactive TORC1 signaling.

We therefore tested whether Pbp1 might induce autophagy via negative regulation of TORC1 signaling. Treatment with rapamycin completely restored autophagy (Figure 1E) and reversed the increased growth of Pbp1-deficient cells in SL medium (Figure 1F), suggesting that these phenotypes are indeed mediated through TORC1. To assess whether the rapamycin-reversible phenotypes of *pbp1Δ* cells are due to increased TORC1 activity, we examined phosphorylation of TORC1-dependent substrates, Sch9, Atg13, Gln3, and Npr1. Each protein exhibited increased phosphorylation in *pbp1Δ* cells compared to WT following the switch to SL medium (Figure 1G).

We next performed a proteomic survey to investigate the basis of the increased growth of *pbp1Δ* mutants in SL medium. Using a SILAC (stable-isotope labeling by amino acids in cell culture) experiment, we found the proteins that were most significantly increased in *pbp1Δ* cells in SL medium were enzymes involved in anabolic metabolism and biosynthesis (Figures S1D and S1E; Table S1). In particular, proteins involved in ribosome biogenesis were significantly increased in abundance in *pbp1Δ* cells (Figure S1F; Table S2). Thus, the increased abundance of proteins involved in translation and anabolic biosynthesis was also consistent with the reporters of increased TORC1 activity in *pbp1Δ* cells. Taken together, these data suggest that *pbp1Δ* cells have hallmarks of hyperactive TORC1 signaling, and Pbp1 is therefore a negative regulator of TORC1.

Pbp1 Interacts with TORC1 Specifically during Respiratory Growth

We next tested whether Pbp1 might interact with components of TORC1 as a possible mechanism of regulation. Taking into account growth conditions in which Pbp1 is required for autophagy, we observed that endogenous Kog1, the yeast ortholog of RAPTOR, co-immunoprecipitated with Pbp1 exclusively in the minimal lactate medium (SL), but not in minimal glucose medium (SD) (Figure 2A). Moreover, this interaction between Pbp1 and Kog1 in SL medium was substantially decreased following switch back to glucose medium (SD) (Figure 2B). In *pbp1Δ* cells, more TORC1 appeared associated with vacuolar membranes as assessed by imaging of Kog1-GFP expressed at an endogenous level (Figure S2A). Therefore, the association between Pbp1 and Kog1 is responsive to cellular metabolic conditions and is more prominent when cells are grown in a non-fermentable carbon source. Increased association between Pbp1 and TORC1 under these conditions is consistent with inhibition of TORC1 and reduced vacuolar localization.

To identify the region within Pbp1 required for binding to TORC1, we constructed a series of deletion mutants of Pbp1 (Figure 2C) and tested their ability to co-immunoprecipitate Kog1. Pbp1 possesses two putative RNA-binding domains, Like SM (Lsm) and Lsm associated domain (LsmAD), near its N-terminus, with the remainder of the protein having no predicted secondary structure (Figure 2C). Pbp1 mutants lacking one or both RNA-binding domains (Figure 2C, mutants 3, 4, 5) retained the ability to interact with Kog1 (Figure 2D). The addition of RNase A to lysates also did not affect the interaction between Pbp1 and Kog1 (Figure S2B). The mutants lacking the RNA-binding

(G) Phosphorylation of endogenously tagged Sch9, Atg13, Gln3, and Npr1 at the indicated time points before and after switch to SL medium. Phosphorylated species exhibit reduced migration during SDS-PAGE. Sch9 samples were analyzed using phos-tag SDS-PAGE. Rapamycin and cycloheximide (CHX) treatment were used to assess the migration of low and high phosphorylated states of these substrates. *pbp1Δ* mutant cells exhibited increased phosphorylation of TORC1 substrates following switch to SL medium.

See also Figure S1 and Table S1.

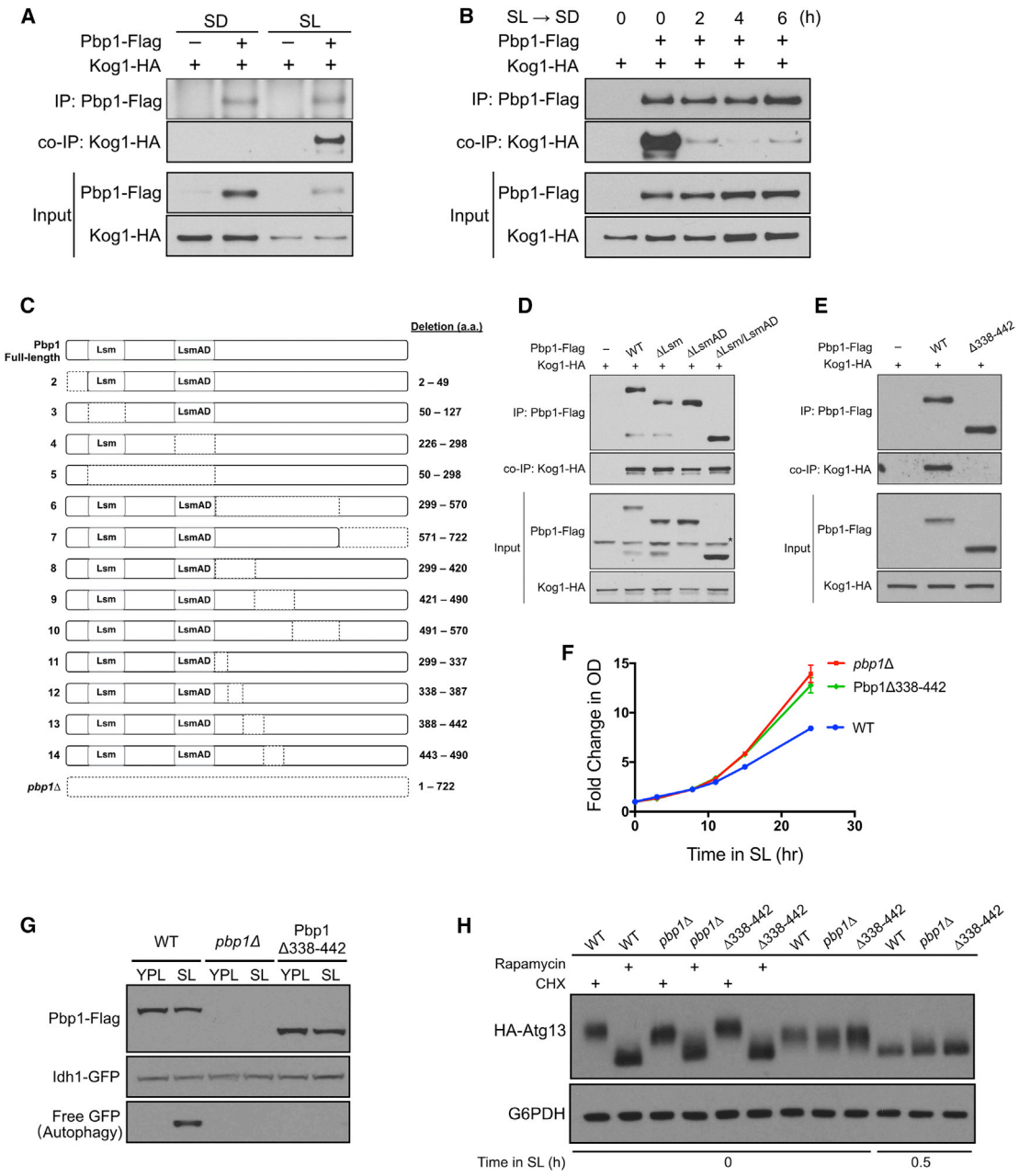

Figure 2. Pbp1 Binds to TORC1 Specifically during Respiratory Growth Independent of Its Putative RNA-Binding Domains

(A) Pbp1 interacts with TORC1 component Kog1 in cells grown in SL, but not SD medium. Cells with endogenously tagged Pbp1 and Kog1 grown in YPL medium were switched to SD or SL medium for 3 h. Flag-tagged Pbp1 in cell lysates was immunoprecipitated with an anti-Flag antibody. Co-immunoprecipitation of Kog1-HA was detected by immunoblotting with anti-HA antibody.

(B) Reduced interaction between Pbp1 and Kog1 following glucose repletion. Cells with endogenously tagged Pbp1 and Kog1 were switched from YPL to SL medium for 3 h and then switched back to SD medium for the indicated times. Immunoprecipitation was performed as described in (A).

(C) Schematic representation of Pbp1 deletion mutants. Dotted lines indicate the deleted region. These deletion mutants were assayed for their ability to interact with Kog1 (D and S2E).

(D) Pbp1 variants lacking individual or both RNA-binding domains could still interact with Kog1. Cells were switched from YPL to SL medium for 3 h and immunoprecipitation was performed as described in (A). Asterisk indicates a non-specific band.

(E) Pbp1 mutant lacking aa 338–442 (Pbp1Δ338–442) was unable to interact with Kog1. Cells were switched from YPL to SL medium for 3 h and immunoprecipitation was performed as described in (A).

(F) Pbp1Δ338–442 exhibited similar growth compared to *pbp1Δ* cells in SL medium. Data were mean ± SD from 3 independent experiments.

(G) GFP cleavage assay. Cells expressing Pbp1Δ338–442 exhibited reduced autophagy after switching to SL medium.

(H) Pbp1Δ338–442 showed increased phosphorylation of endogenously tagged Atg13 similar to *pbp1Δ* cells.

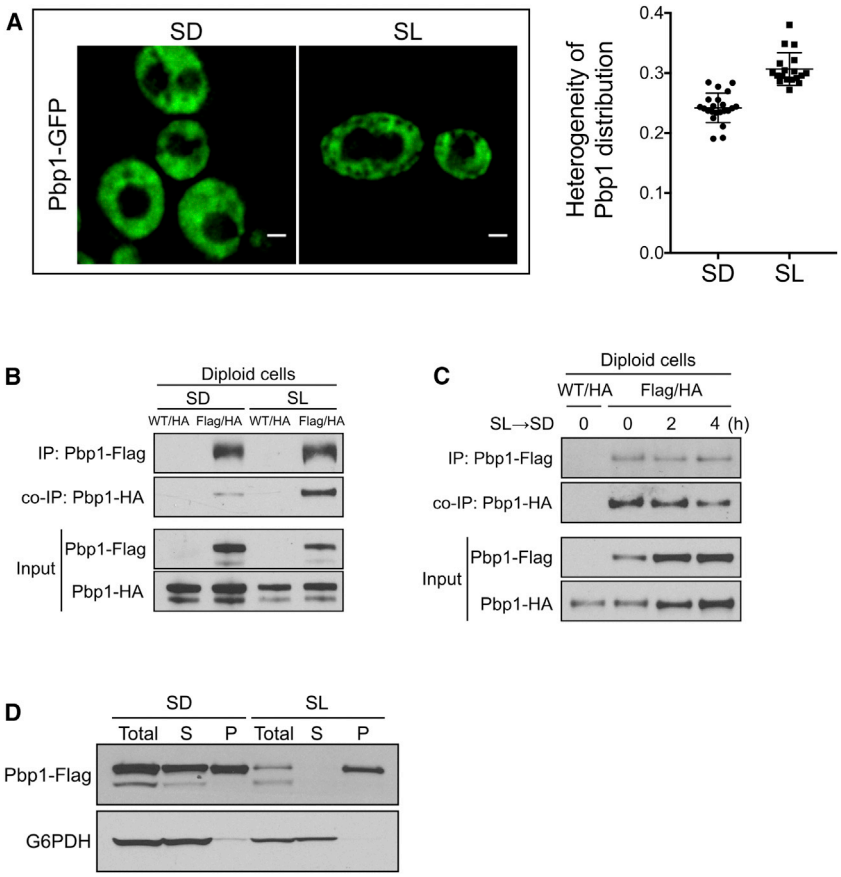

Figure 3. Pbp1 Self-Associates into Pelletable Assemblies during Respiratory Growth

(A) Images of cells expressing Pbp1-GFP from the endogenous chromosomal locus. Images were taken after switch to SD for 8 h or SL for 6 h. Note that Pbp1 is distributed more heterogeneously in cells growing in SL medium. Scale bar, 1 μm. Plot comparing standard deviation/mean of Pbp1-GFP intensity in individual cells grown in SD versus SL ($p = 6 \times 10^{-8}$, two-sample Kolmogorov-Smirnov test).

(B) Pbp1 self-associates in cells grown in SL medium. Diploid cells with endogenously Flag- and HA-tagged *PBP1* alleles were switched from YPL to SD or SL medium for 6 h. Flag-tagged Pbp1 in cell lysates was precipitated with an anti-Flag antibody. Co-immunoprecipitation of Pbp1-HA was detected by immunoblotting with anti-HA antibody.

(C) Pbp1 self-association is decreased after glucose repletion. Diploid cells with endogenously Flag- and HA-tagged *PBP1* alleles were switched from YPL to SL for 3 h and then switched back to SD medium for indicated times. Immunoprecipitation was performed as described in (B).

(D) Pbp1 is present primarily in the pellet fraction in cells grown in SL medium. Cells with endogenously tagged Pbp1 grown in YPL were switched to SD or SL medium for 6 h. Lysed cells were centrifuged for 1 h at 100,000 × *g* for separating supernatant (S) and pellet (P).

See also Figure S3 and Video S1.

domains also did not affect autophagy or growth (Figures S2C and S2D).

We then tested the ability of other Pbp1 truncation mutants to co-immunoprecipitate Kog1 (Figure S2E). We observed that the interaction between Pbp1 and Kog1 is mediated through a ~100 amino acid region (aa 338–442) downstream of the two putative RNA-binding domains (Figures 2E and S2E, mutants 6, 8, 9, 12, 13). Pbp1 mutants lacking this region exhibited the same increased growth and defective autophagy phenotype as the *pbp1Δ* mutant (Figures 2F and 2G), as well as increased phosphorylation of the TORC1-responsive substrate Atg13 (Figure 2H). These data demonstrate that an interaction between Pbp1 and Kog1 is required for the inhibition of TORC1 during respiratory growth.

Pbp1 Self-Associates to Form Nebulous Assemblies

To further investigate how Pbp1 regulates TORC1 signaling, we examined a possible link to Pbp1 as a component of stress granules (Buchan et al., 2008). Under severe heat stress, Pbp1 was reported to sequester TORC1 in foci-like stress granules, which prevent TORC1 activation (Takahara and Maeda, 2012). However, in cells expressing normal amounts of Pbp1-GFP, Pbp1 did not form any structures reminiscent of defined, foci-like granules in SL medium (Figure 3A). Two other stress granule markers, Pab1 and Pub1, also did not localize to foci-like granules in SL medium as compared to the glucose-deprivation medium (Figure S3A). Instead, Pbp1 exhibited a non-uniform distribution, and the protein appeared to be present in the form of dynamic, nebulous assemblies throughout the cell, reminiscent of a condensate (Banani et al., 2017) (Figure 3A; Video S1). Treatment of cells with 1,6-hexanediol, an alcohol commonly used to disrupt weak hydrophobic interactions and disturb phase separation (Lin et al., 2016; Molliex et al., 2015; Ribbeck and Görlich, 2002; Romero et al., 2007), caused the distribution of Pbp1 to become more uniform, further consistent with the idea that it forms a condensate *in vivo* (Figure S3B). Cycloheximide, which reportedly inhibits stress granule formation, did not change the distribution pattern of Pbp1 within cells (Figure S3C). Interestingly, in glucose medium, Pbp1 exhibited a more uniform distribution throughout the cytoplasm (Figure 3A).

It has previously been suggested that Pbp1 has the potential to homo-multimerize (Mangus et al., 1998), which could explain its ability to form assemblies (Figure 3A). Using diploid cells expressing two different epitope-tagged versions of Pbp1, we examined the ability of Pbp1 to self-interact as assessed by co-immunoprecipitation from cell extracts. Pbp1 was strongly self-associated in extracts from cells grown in SL medium, in contrast to cells grown in SD (Figure 3B). Furthermore, the addition of glucose to cells growing in SL medium gradually reduced the ability of Pbp1 to self-associate (Figure 3C). Therefore, the ability of Pbp1 to interact with both itself and Kog1 is dynamic and responsive to cellular metabolic state.

Fractionation experiments showed that in cells grown in SL medium, the majority of Pbp1 protein was present in the pellet

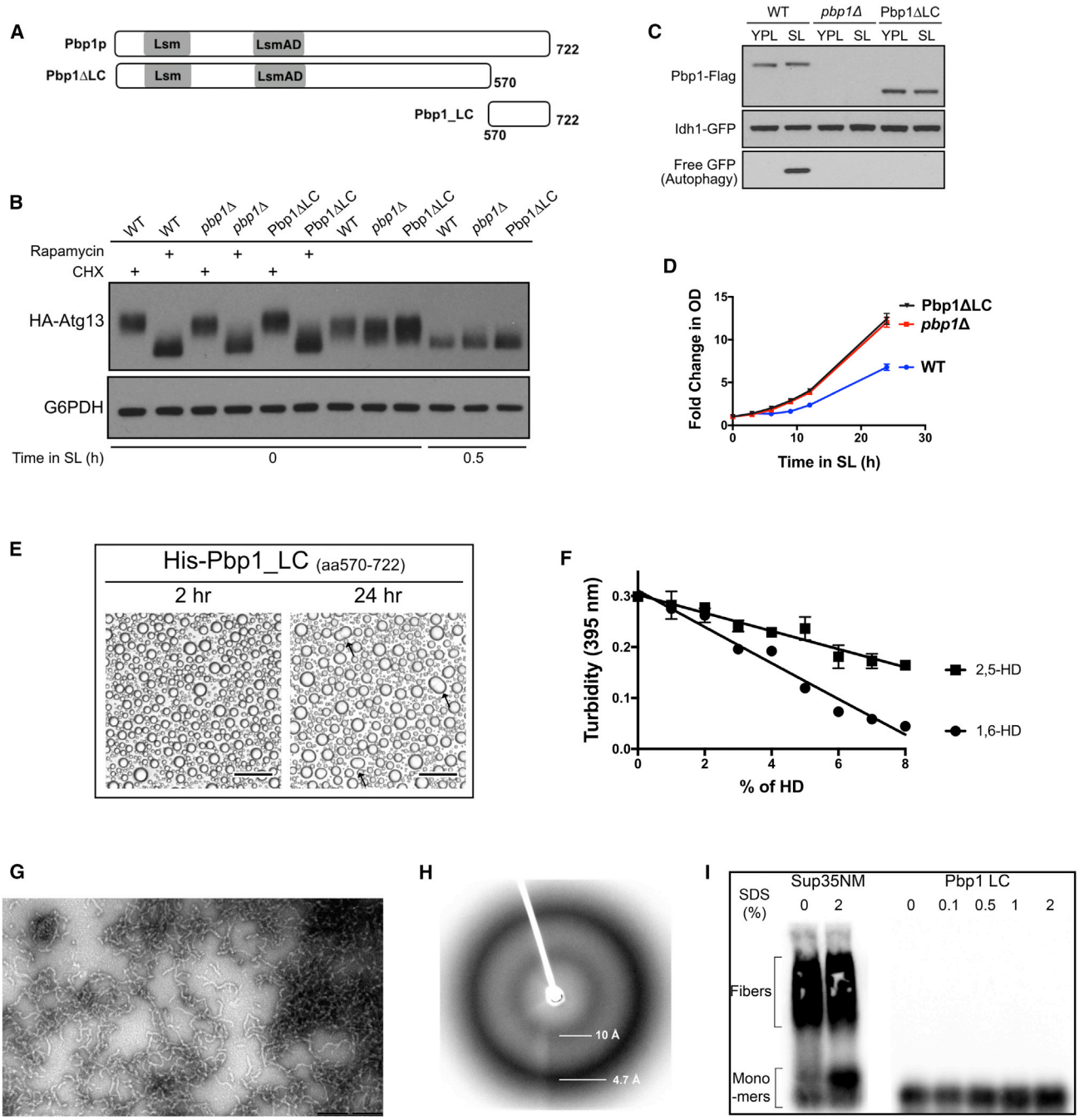

Figure 4. The C-Terminal Low-Complexity Region of Pbp1 Can Phase Separate and Is Required for Inhibition of TORC1

(A) Schematic of domains present in Pbp1. Pbp1ΔLC lacks the C-terminal LC region, and Pbp1_LC denotes the C-terminal low-complexity (LC) region alone.

(B) Cells expressing Pbp1ΔLC exhibited increased phosphorylation of endogenously tagged Atg13 similar to *pbp1Δ* cells.

(C) GFP cleavage assay showing cells expressing Pbp1ΔLC completely lost the ability to induce autophagy following switch to SL medium.

(D) Growth curves showing cells expressing Pbp1ΔLC exhibited similar growth compared to *pbp1Δ* cells.

(E) Phase-separated droplet formation by purified His_6-Pbp1_LC (2 mg/mL, ~100 μM). Images were taken 2 h and 24 h after lowering the salt concentration. Arrows indicate fused droplets that did not return to a spherical shape. Scale bar, 50 μm

(F) Dissolution of His_6-Pbp1_LC phase-separated droplets by aliphatic alcohols. Turbidity changes of the phase-separated droplet solution containing the indicated concentration of 1,6-hexanediol (HD) or 2,5-HD were measured by light absorbance at 395 nm. Note that the droplets were more sensitive to 1,6-HD. Data were mean ± SD from 3 independent experiments.

(G) Electron micrographs of GFP-Pbp1_LC fibrils. Pbp1_LC formed uniformly similar, polymeric fibrils. Scale bar, 500 nm.

(legend continued on next page)

fraction, consistent with the idea that it may form large protein assemblies under such conditions (Figure 3D). However, in cells grown in glucose, substantial amounts of Pbp1 were present in the soluble fraction, in addition to the pellet fraction (Figure 3D). Taken together, these observations indicate that at normal expression levels and physiological temperatures, Pbp1 does not form foci-like granules and is instead present in the form of pelletable assemblies during respiratory growth, which may play a role in the negative regulation of TORC1.

A C-Terminal Low-Complexity Region of Pbp1 that Phase Separates Is Required for Inhibition of TORC1

We next tested whether other regions of Pbp1 were required for self-association and perhaps the inhibition of TORC1. It has been noted that Pbp1 possesses a methionine- and proline-rich C-terminal region (Mangus et al., 1998). Sequence analysis of this region revealed that it is of low-complexity (LC) (Figure S4A), which is a feature of proteins that have a tendency to self-assemble or aggregate (Han et al., 2012; Molliex et al., 2015). To determine whether this region of Pbp1 might be necessary for regulating TORC1 signaling, we constructed a Pbp1 mutant lacking the C-terminal low-complexity region (Pbp1ΔLC) (Figure 4A). Upon assessment of its function *in vivo*, this mutant exhibited increased phosphorylation of Atg13 (Figure 4B), reduced autophagy (Figure 4C), and an increased growth phenotype indistinguishable from *pbp1Δ* cells (Figure 4D).

To assess the biochemical features of this LC region, we recombinantly expressed and purified a fragment comprising this portion of Pbp1 (Pbp1_LC, aa570-722) (Figure 4A). Upon lowering the salt concentration to physiological levels, this purified fragment readily phase-separated into droplets *in vitro* (Figure 4E), and the droplets were stable within the time observed. In addition, these Pbp1_LC droplets were sensitive to 1,6-hexanediol. The droplets exhibited higher sensitivity to 1,6-hexanediol compared to 2,5-hexanediol (Figure 4F), which can be a property of proteins that phase separate (Kroschwald et al., 2015; Lin et al., 2016; Shi et al., 2017).

Using electron microscopy, we further observed that purified Pbp1_LC could readily form fibrils of 15–20 nm in width (Figure 4G). Consistent with the phase-separated droplets, these fibrils were also more sensitive to 1,6-hexanediol (Figure S4B). X-ray diffraction analysis of Pbp1_LC yielded a characteristic diffraction pattern with circular reflections at 4.7 Å and 10 Å, indicating that the fibrils are of cross-β structure (Figure 4H) (Astbury et al., 1935; Geddes et al., 1968; Sunde and Blake, 1997). These Pbp1_LC fibrils were highly labile and completely disassembled upon incubation at 37°C in the absence of SDS, in contrast to fibers formed by the yeast prion protein Sup35 (Figure 4I). Taken together, these observations suggest that the C-terminal LC region of Pbp1 has a propensity to self-associate into reversible, higher-order assemblies of cross-β structure.

The C-Terminal LC Region Enables Pbp1 to Self-Associate and Form a Perimitochondrial Condensate *In Vivo*

We next examined whether this C-terminal LC region of Pbp1 enables its self-association in cells. We expressed a variant of Pbp1 lacking the C-terminal LC region (Pbp1ΔLC) in diploid cells with two different tags and assayed self-association using immunoprecipitation. In contrast to full-length Pbp1, Pbp1ΔLC showed reduced ability to self-associate (Figure 5A). Moreover, the Pbp1ΔLC mutant was less concentrated in the pellet after fractionation (Figure 5B).

Pbp1ΔLC also exhibited a more uniform distribution pattern throughout the cytosol compared to full-length Pbp1 protein (Figure 5C). When the C-terminal LC region of Pbp1 alone was expressed in cells, we observed that it formed punctate-like structures in both lactate and glucose medium (Figure 5D). Interestingly, these Pbp1_LC puncta were perimitochondrial (Figure 5D). Full-length Pbp1 did not co-localize with organelles such as the vacuole or endoplasmic reticulum (Figure S5). However, using a mitochondrial DsRed marker, we observed that Pbp1 appeared to be proximal, but exclusive of the mitochondria (Figure S5). Therefore, the C-terminal LC region of Pbp1 may enable the protein to form a nebulous condensate proximal to the mitochondria. Collectively, these results suggest that the propensity of the C-terminal LC region to phase separate may explain the non-uniform distribution of full-length Pbp1, its ability to self-associate to form pelletable assemblies, as well as its ability to inhibit TORC1 *in vivo*.

Methionine Residues in the C-Terminal LC Region of Pbp1 Influence Stability of Phase Separation and Are Critical for Inhibition of TORC1

Sequence analysis of the Pbp1 C-terminal LC region revealed an unusually high frequency of methionine residues (24 methionines in 150 aa) compared to the rest of the yeast proteome (Figures 6A and 6B). To test the importance of these methionines, we constructed a series of C-terminal truncation mutants lacking increasing numbers of methionine residues (Figure 6C) and examined their ability to induce autophagy in SL medium (Figure 6D).

We observed that a Pbp1 mutant lacking a region containing the last 8 methionines (M_{17}–M_{24}) (Figure 6C, mutant (2)) could still induce autophagy, but further deletion of a region that contains M_{11}–M_{16} significantly reduced autophagy (Figure 6D), suggesting the importance of this subset of methionines for function. By mutating pairs of adjacent methionine residues among M_{11}–M_{16} to serine, we observed that Pbp1_LC $M_{11,12}$ → S exhibited the weakest ability to form fibrils *in vitro* (Figure S6A). We therefore mutated M_{11}, M_{12}, and immediately upstream and downstream methionine residues to serine, to generate a series of mutants containing 2, 4, 6, or 8 M → S mutations.

Strikingly, increasing the number of M → S substitutions within this region gradually reduced the ability of Pbp1 to induce

(H) X-ray diffraction pattern of His_6-Pbp1_LC polymer pellets. Clear X-ray reflections were observed at 4.7 Å and 10 Å indicative of a cross-β structure.
(I) SDD-AGE analysis of yeast Sup35 NM amyloid polymers and His_6-Pbp1_LC polymers. SDS exposure did not substantially affect ySup35 NM amyloid polymers whereas Pbp1_LC polymers were fully depolymerized under all conditions.
See also Figure S4.

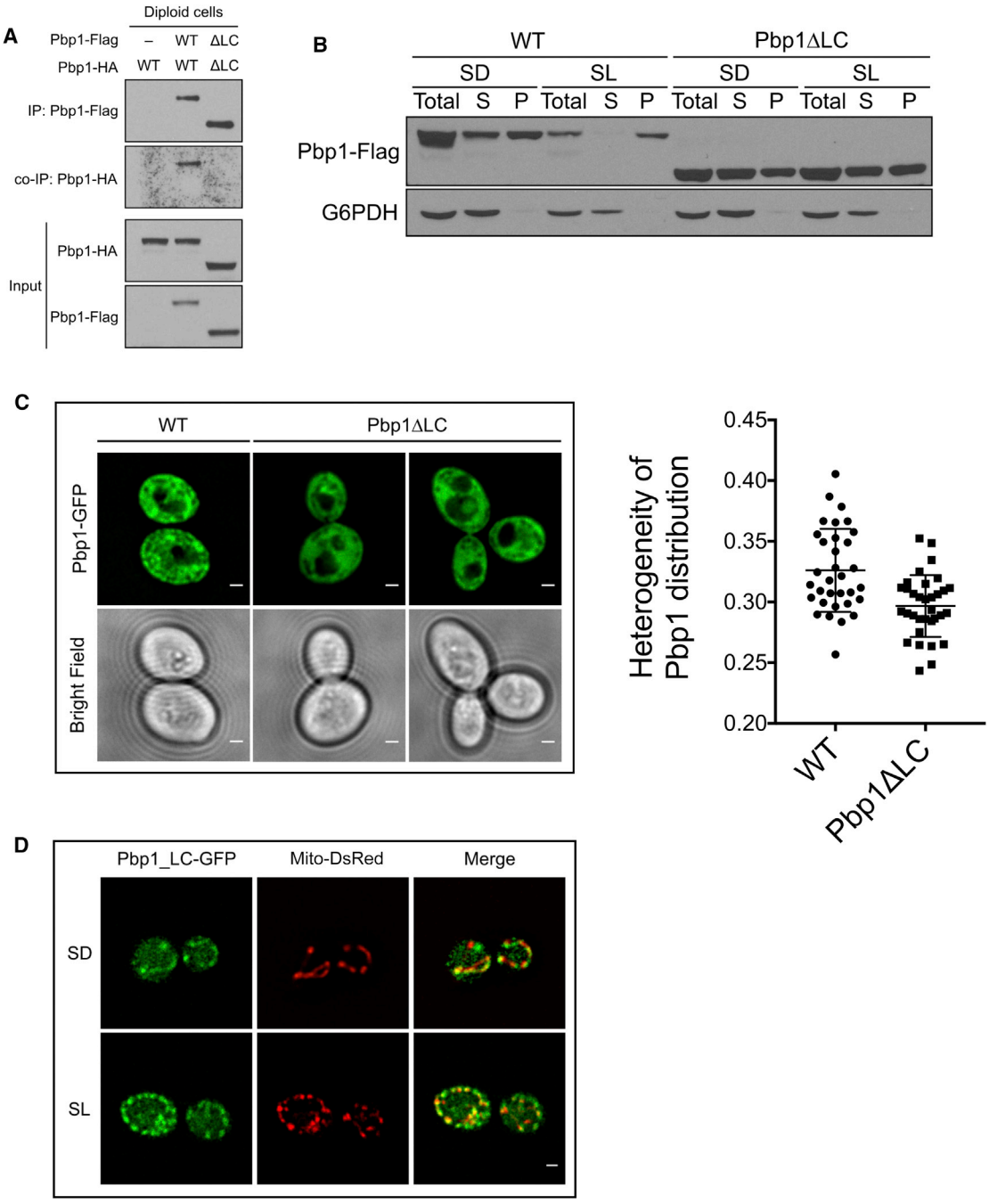

Figure 5. The Ability of Pbp1 to Self-Associate Is Mediated by the C-Terminal Low Complexity Region

(A) Pbp1ΔLC cannot self-associate in cells grown in SL medium. Diploid cells expressing endogenously Flag- and HA-tagged Pbp1ΔLC alleles were switched from YPL to SL medium for 3 h. Flag-tagged Pbp1ΔLC in cell lysates was precipitated with an anti-Flag antibody. Co-immunoprecipitation of Pbp1ΔLC-HA was detected by immunoblotting with anti-HA antibody.

(B) Western blot showing the distribution of Pbp1 WT and Pbp1ΔLC variant in SD or SL medium. Pbp1ΔLC was less concentrated in the pellet fraction in SL medium. Cells were cultured and processed as described in Figure 3D.

(C) Images of cells expressing Pbp1-GFP or Pbp1ΔLC-GFP at endogenous levels in SL medium. Note that Pbp1ΔLC exhibited a more uniform distribution pattern throughout the cytosol. Plot comparing the heterogeneity of Pbp1 distribution (SD/mean) in individual cells expressing either Pbp1-GFP or Pbp1ΔLC-GFP ($p = 0.0185$, two-sample Kolmogorov-Smirnov test).

(D) Images of cells expressing Pbp1_LC-GFP at endogenous levels and the mitochondria-targeted RFP reporter (mt-DsRed) in SD and SL medium. Note that Pbp1_LC formed punctate-like structures that appear perimitochondrial in both media. Scale bar, 1 μm.

See also Figure S5.

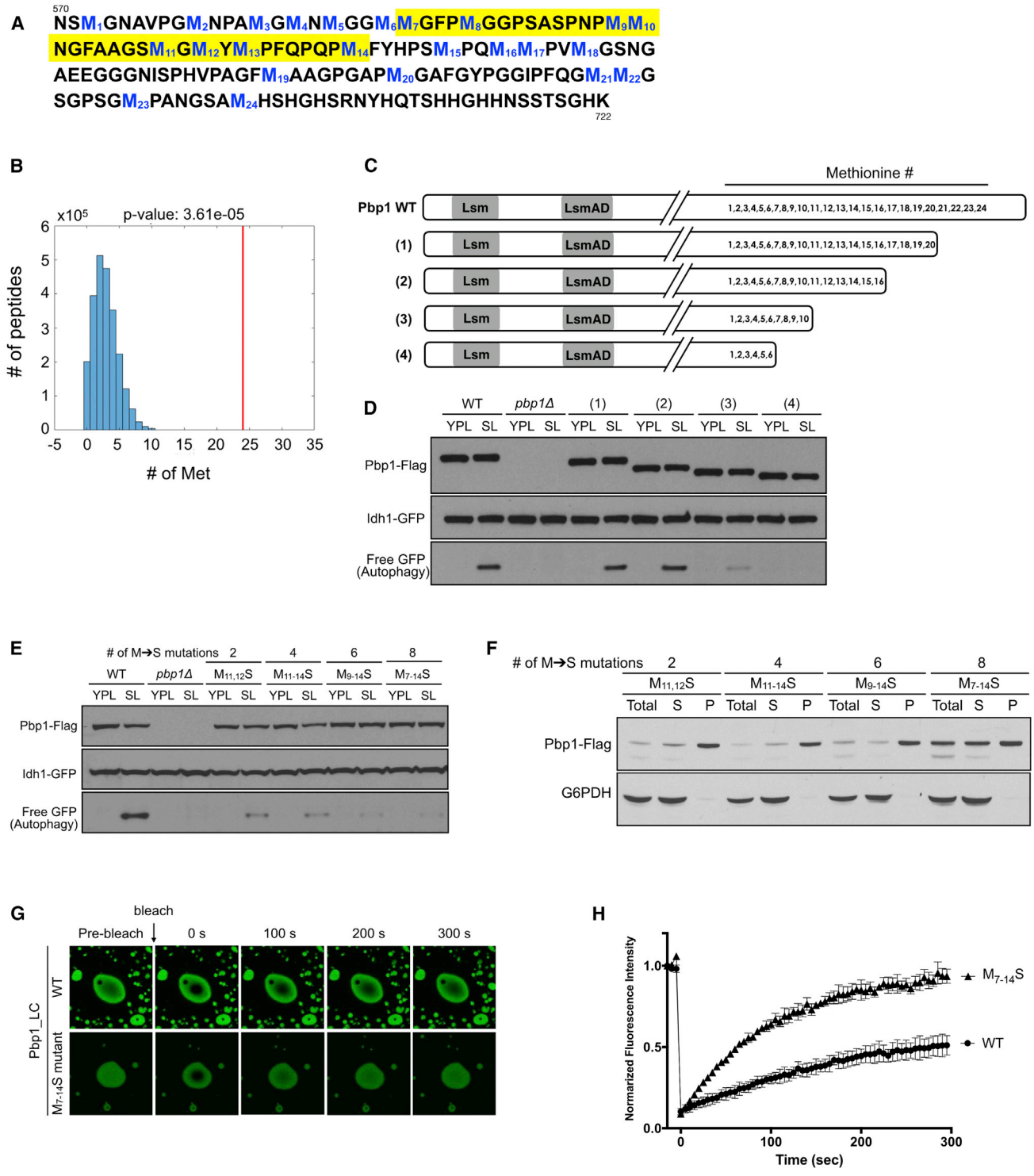

Figure 6. Methionine Residues in the C-Terminal LC Region of Pbp1 influence Stability of Phase Separation and Are Critical for Inhibition of TORC1

(A) Amino acid sequence of the Pbp1 C-terminal LC region. The 24 methionine residues are numbered and highlighted in blue. The yellow highlighted region denotes the critical methionine residues for function deduced from the experiments below.

(B) The C-terminal low complexity region of Pbp1 has unusually high methionine content compared to the rest of the yeast proteome. Plot showing methionine content per 150 amino acids across the yeast proteome. Individual proteins were analyzed using a sliding window of a length of 150 aa, and the number of

(legend continued on next page)

autophagy in cells. In particular, the $M_{7–14}S$ mutant exhibited severely reduced autophagy (Figure 6E). Moreover, this mutant protein was less concentrated in the pellet fraction, with a substantial amount instead present in the soluble fraction (Figure 6F).

We then tested the effect of increasing numbers of methionine mutations on phase-separated droplet formation of the LC region. All of the mutant combinations tested still phase-separated into droplets (Figure S6B). However, variants harboring increasing numbers of methionine mutations significantly decreased the stability of phase separated droplets as the droplets dissolved more readily upon lowering the protein concentration (Figure S6C). Using a fluorescence recovery after photobleaching (FRAP) assay, we observed that the Pbp1_LC $M_{7–14}S$ droplets were able to recover much faster compared to WT droplets (Figures 6G and 6H; Videos S2 and S3), consistent with their decreased stability. Therefore, the functional WT Pbp1_LC region exhibits slower FRAP and is more solid-like, whereas a non-functional mutant *in vivo* exhibits faster FRAP and is more liquid-like. Taken together, we observed a strong correlation between the stability of phase-separated droplets *in vitro* and the ability of the protein to sediment to the pellet and induce autophagy in cells.

Pbp1 Is Important for Maintaining Cellular Fitness and Mitochondrial Function

Cells lacking Pbp1 bypass autophagy and continue to grow inappropriately under conditions that require mitochondrial respiration. To investigate the physiological consequences of loss of Pbp1, we measured the cell division times of more than 1,000 WT and *pbp1Δ* cells as they replicatively age in SL medium using a microfluidic device. Newly born *pbp1Δ* daughter cells exhibited a shorter G1 phase (Figure 7A), which is consistent with the increased growth phenotype in batch cultures (Figure 1D). However, after the first few divisions, *pbp1*Δ mother cells displayed significantly protracted division times in comparison to WT mother cells (Figure 7B). In contrast, when *pbp1Δ* cells were grown in glucose, their division times were comparable to WT even after many divisions (Figure S7A). Moreover, there were substantially more *pbp1Δ* cells that appeared replicatively senescent (>2,000 min between divisions) (Figure 7C) or with abnormal morphology (Figures 7D and S7B).

To examine a possible role for Pbp1 in maintaining mitochondrial function, we grew WT and *pbp1Δ* cells in SL medium to stationary phase as a means of chronic nutritional stress. After a prolonged period in stationary phase, *pbp1Δ* cells produced significantly more petites (Figure 7E), suggesting that many cells gradually lost mitochondrial respiratory function, as well as reduced survivability (Figure 7F). It thus appears that mitochondrial dysfunction and cell death may emerge due to loss of Pbp1 following prolonged metabolic or nutritional stress, or as a function of age. Consistent with this idea, the abundance of Pbp1 appears to decrease substantially in replicatively aged cells (Janssens et al., 2015). Pbp1 may therefore sense respiratory status and mitochondrial dysfunction to properly modulate TORC1 signaling.

DISCUSSION

In this study, we show that Pbp1 is a bona fide negative regulator of TORC1 signaling whose function becomes especially important when cells heavily utilize mitochondria for energy production. Loss of Pbp1 function most prominently results in phenotypes associated with hyperactive TORC1 signaling, which include the inhibition of autophagy and increased anabolic metabolism due to promoting the biosynthetic functions of mitochondria (Chen et al., 2017). There has been a lack of clarity regarding the normal physiological function of Pbp1. Previous studies have implicated the protein in various aspects of RNA processing and as a component of stress granules (Buchan et al., 2008; Mangus et al., 1998; Swisher and Parker, 2010). However, during respiratory growth under physiological temperatures and expression levels, we find no evidence that Pbp1 forms discrete, punctate-like bodies that are typically associated with stress granules. Instead, it forms a more disperse condensate whose properties are dependent on the metabolic state. When cells are growing in lactate, Pbp1 is almost exclusively in the pellet fraction and exhibits a more non-uniform localization throughout the cytosol. With the ability to associate with Kog1, this form of Pbp1 appears to be capable of inhibiting the TORC1 complex.

However, we further identified an unusual, methionine-rich low complexity region of Pbp1 that is also required for the inhibition of TORC1. This LC region readily phase separates to form droplets *in vitro*. Mutational analysis revealed a specific subset of methionine residues that weaken phase separation. Importantly, these same methionines are critical for inhibition of TORC1 and induction of autophagy *in vivo*. Taken together, our findings reveal how Pbp1 inhibits TORC1 through an unconventional

methionines was counted for each 150 aa window. The number of 150 aa peptides (y axis) with indicated numbers of methionine residues (x axis) was plotted. Red line indicates the position of the Pbp1 C-terminal LC region (24 methionines).

(C) Schematic representation of a series of C-terminal truncation mutants lacking increasing numbers of methionine residues.

(D) GFP cleavage assay showing autophagy in cells expressing the mutants depicted in (C). Cells expressing Pbp1 mutants lacking the region containing M_{11} to M_{16} (mutant (3), (4)) showed reduced autophagy.

(E) GFP cleavage assay showing autophagy in cells expressing Pbp1 mutants with indicated methionine to serine point mutations. Cells expressing Pbp1 with 8 methionine mutations ($M_{7–14}$ S) showed severely reduced autophagy.

(F) Western blot showing the distribution of Pbp1 mutant proteins with indicated methionine to serine mutations in SL medium. The Pbp1 protein containing 8 methionine mutations ($M_{7–14}$ S) was less concentrated in the pellet fraction. Cells were cultured and processed as described in Figure 3D.

(G) FRAP (fluorescence recovery after photobleaching) analysis of phase-separated droplets formed by purified Pbp1_LC WT or M_{7-14} S variant (~100 μM). See also Videos S2 and S3.

(H) Quantification of FRAP in (G). Note the phase-separated droplets of Pbp1_LC $M_{7–14}$ S recovered faster compared to WT. Plots are generated from 9 droplets in 3 independent experiments.

See also Figure S6.

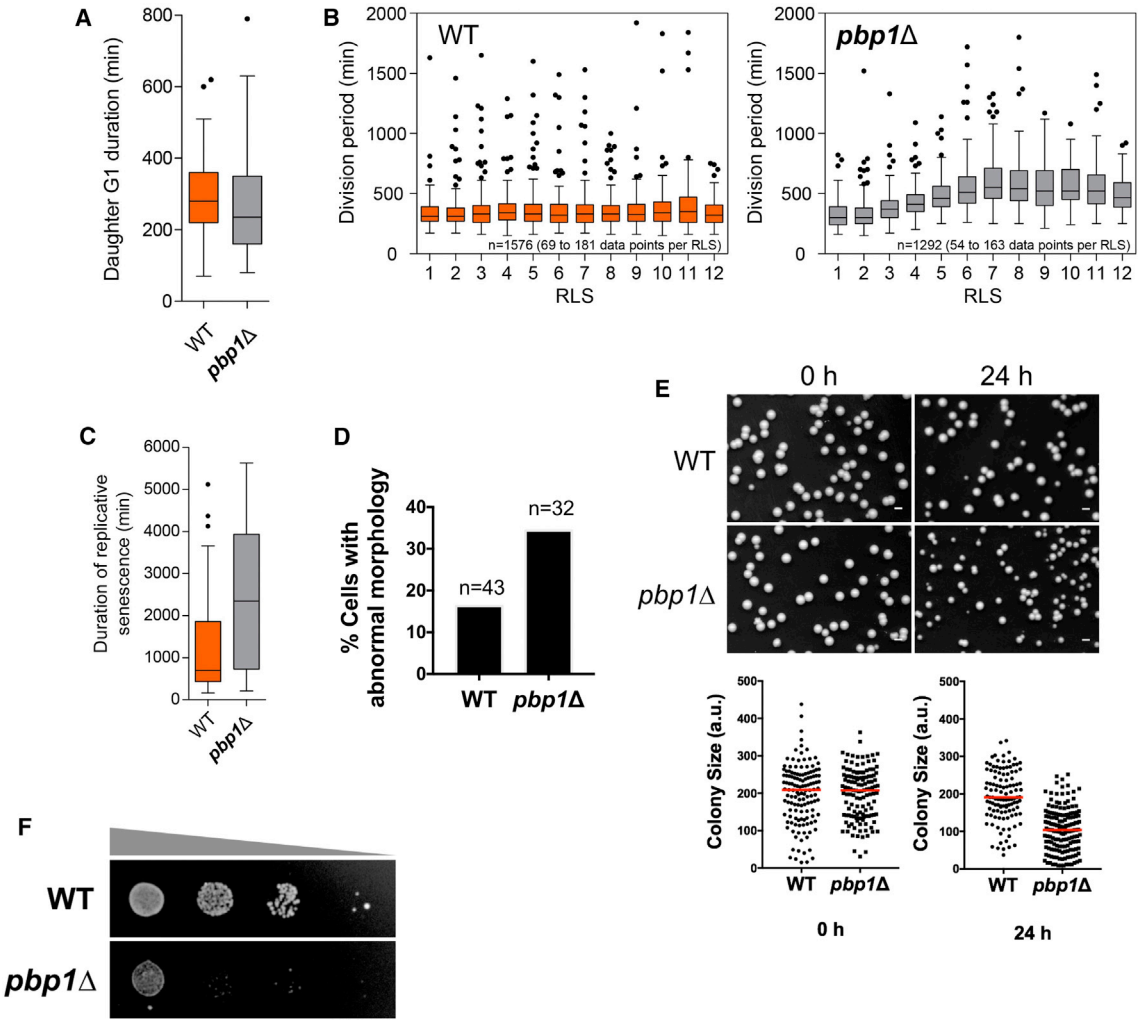

Figure 7. Pbp1 Is Important for Maintaining Cellular Fitness and Mitochondrial Function

(A) Newly born *pbp1Δ* cells exhibited a shorter G1 phase in SL medium. Boxplots showing the duration of G1 in WT (n = 51) and *pbp1Δ* (n = 44) daughter cells.

(B) *pbp1Δ* cells exhibited protracted division times after the first few divisions in SL medium. The division period was plotted against replicative lifespan (RLS) for WT and *pbp1Δ* cells. Each boxplot contains data from n = 69–181 and n = 54–163 for WT and *pbp1Δ* cells, respectively. In total, data from 1,576 (WT) and 1,292 (*pbp1Δ*) division events were recorded.

(C) Boxplots showing the duration of replicative senescence in WT (n = 43) and *pbp1Δ* (n = 34) cells.

(D) More *pbp1Δ* cells (11 in 32) displayed abnormal morphology at terminal stage compared to WT cells (7 in 43).

(E) *pbp1Δ* cells produced significantly more petites after a prolonged period in stationary phase. Cells were switched from YPL to SL medium, and grown to stationary phase. ~350 cells were plated onto YPD at indicated time points after entering stationary phase. Colony sizes were analyzed using ImageJ. Scale bar, 0.2 cm.

(F) Spotting assay on SL plates showing the survivability of WT and *pbp1Δ* cells at 24 h after stationary phase. Note that *pbp1Δ* cells exhibited reduced survivability compared to WT.

See also Figure S7.

mechanism involving phase separation. The C-terminal LC region enables Pbp1 to form an intracellular condensate, which is required for inhibiting TORC1 during respiratory growth. TORC1 still appears present at vacuoles in SL medium, but at reduced amounts compared to *pbp1Δ* cells (Figure S2A), which is potentially consistent with a physical sequestration model of inhibition (Takahara and Maeda, 2012). However, because a portion of the protein outside of the C-terminal LC region mediates actual binding to TORC1 (Figures 2E and S2E), we propose that an additional mechanism linked to phase separation of the LC region is required for the inhibition of TORC1, perhaps through modulation of distinct conformational or oligomeric states of TORC1 (Prouteau et al., 2017).

Ataxin-2 is the mammalian ortholog of yeast Pbp1. Polyglutamine expansions near the N terminus of human ataxin-2 are linked to both ALS and spinocerebellar ataxia. However, just

like yeast Pbp1, the normal physiological function of ataxin-2 remains unclear (Alves-Cruzeiro et al., 2016; Carmo-Silva et al., 2017; Lastres-Becker et al., 2008). Mutants lacking ataxin-2 have been constructed in multiple species and exhibit several phenotypes consistent with those reported here for Pbp1 as a negative regulator of TORC1. These include increased ribosomal protein amounts (Fittschen et al., 2015) and increased body size of dietary-restricted animals that is accompanied by more rapid animal development (Bar et al., 2016). In addition, ataxin-2 has been reported to cross-talk with disease-associated proteins such as C9orf72 and Gr2b (growth factor receptor-bound protein 2), pointing to putative functions in autophagy and nutrient signaling (Drost et al., 2013; Sellier et al., 2016). Consistent with results herein, a recent report also demonstrates that a C-terminal intrinsically disordered region of ataxin-2 mediates the formation of RNP granules in *Drosophila* cells (Bakthavachalu et al., 2018). Our findings on the function and consequences of loss of Pbp1 in yeast suggest that compromising ataxin-2 function in neurons might result in mitochondrial dysfunction, energetic crisis, and eventually apoptosis, hallmarks that have all been linked to neurodegenerative disease (Nixon, 2013; Tatton and Olanow, 1999).

Last, why might an intracellular condensate be required to regulate TORC1 specifically during respiratory growth? In addition to ATP synthesis, the mitochondria also play a key role in the biosynthesis of nitrogen-containing amino acids, which is promoted by activation of TORC1 (Chen et al., 2017; Laxman et al., 2014). An increased reliance on mitochondria for ATP synthesis leads to an increased dependency on inhibitors of TORC1 to toggle the mitochondria between ATP and biosynthesis modes in tune with the metabolic state or demands of the cell. Because cells lacking Pbp1 begin to exhibit mitochondrial dysfunction and reduced survivability following prolonged nutritional stress or as a function of age under respiratory conditions, we propose that Pbp1 specifically senses some aspect of mitochondrial activity or dysfunction to adjust TORC1 for purposes of sustaining mitochondrial health. In the accompanying paper, we show precisely how the methionine-rich LC region of Pbp1 senses hydrogen peroxide as a signal of mitochondrial dysfunction to subsequently modulate TORC1 signaling for metabolic adaptation (Kato et al., 2019 [this issue of *Cell*]). In closing, our findings have revealed an unanticipated spatial organization and regulation of signaling and metabolism within the cell necessitated by mitochondrial respiration.

STAR★METHODS

Detailed methods are provided in the online version of this paper and include the following:

SUPPLEMENTAL INFORMATION

Supplemental Information can be found online at https://doi.org/10.1016/j.cell.2019.02.043.

ACKNOWLEDGMENTS

We thank K. Luby-Phelps and the UTSW Live Cell Imaging Core Facility for assistance with microscopy experiments. We thank S. McKnight, S. Fu, Y. Kuo, and the Tu Lab for valuable advice and suggestions. B.P.T. is supported by grants from the NIH (R01GM094314), the Welch Foundation (I-1797), the David and Lucile Packard Foundation, and a HHMI-Simons Faculty Scholars Award. M.K. is funded by the support of an anonymous donor to the laboratory of S. McKnight. N.E.W. is supported by Cancer Prevention and Research Institute of Texas (RR150058) and Welch Foundation (I-1919), which were obtained by A. Doncic.

AUTHOR CONTRIBUTIONS

This study was conceived by Y.-S.Y. and B.P.T. M.K. performed *in vitro* assays of phase-separated droplet formation. X.W. originally identified Pbp1 in a visual screen for novel autophagy regulators. A. Litsios and M.H. performed microfluidic imaging and quantitative analysis of cell divisions. A. Lemoff and H.M. performed SILAC analysis. B.M.S. and Y.W. assisted with mutant and strain construction. C.-H.H. assisted with the computational analysis of SILAC proteome data and methionine content. N.E.W. performed image processing analysis of Pbp1 distribution. Y.-S.Y. led and performed all other experiments. The paper was written by Y.-S.Y. and B.P.T.

DECLARATION OF INTERESTS

The authors declare no competing interests.

Received: December 11, 2017
Revised: October 4, 2018
Accepted: February 25, 2019
Published: April 11, 2019

REFERENCES

Alves-Cruzeiro, J.M., Mendonça, L., Pereira de Almeida, L., and Nóbrega, C. (2016). Motor Dysfunctions and Neuropathology in Mouse Models of Spinocerebellar Ataxia Type 2: A Comprehensive Review. Front. Neurosci. *10*, 572.

Ashburner, M., Ball, C.A., Blake, J.A., Botstein, D., Butler, H., Cherry, J.M., Davis, A.P., Dolinski, K., Dwight, S.S., Eppig, J.T., et al.; The Gene Ontology Consortium (2000). Gene ontology: tool for the unification of biology. Nat. Genet. *25*, 25–29.

Astbury, W.T., Dickinson, S., and Bailey, K. (1935). The X-ray interpretation of denaturation and the structure of the seed globulins. Biochem. J. *29*, 2351–2360.

Bakthavachalu, B., Huelsmeier, J., Sudhakaran, I.P., Hillebrand, J., Singh, A., Petrauskas, A., Thiagarajan, D., Sankaranarayanan, M., Mizoue, L., Anderson, E.N., et al. (2018). RNP-Granule Assembly via Ataxin-2 Disordered Domains Is Required for Long-Term Memory and Neurodegeneration. Neuron *98*, 754–766.

Banani, S.F., Lee, H.O., Hyman, A.A., and Rosen, M.K. (2017). Biomolecular condensates: organizers of cellular biochemistry. Nat. Rev. Mol. Cell Biol. *18*, 285–298.

Bar, D.Z., Charar, C., Dorfman, J., Yadid, T., Tafforeau, L., Lafontaine, D.L., and Gruenbaum, Y. (2016). Cell size and fat content of dietary-restricted Caenorhabditis elegans are regulated by ATX-2, an mTOR repressor. Proc. Natl. Acad. Sci. USA *113*, E4620–E4629.

Bar-Peled, L., Chantranupong, L., Cherniack, A.D., Chen, W.W., Ottina, K.A., Grabiner, B.C., Spear, E.D., Carter, S.L., Meyerson, M., and Sabatini, D.M. (2013). A Tumor suppressor complex with GAP activity for the Rag GTPases that signal amino acid sufficiency to mTORC1. Science *340*, 1100–1106.

Boland, B., Kumar, A., Lee, S., Platt, F.M., Wegiel, J., Yu, W.H., and Nixon, R.A. (2008). Autophagy induction and autophagosome clearance in neurons: relationship to autophagic pathology in Alzheimer's disease. J. Neurosci. *28*, 6926–6937.

Boyle, E.I., Weng, S., Gollub, J., Jin, H., Botstein, D., Cherry, J.M., and Sherlock, G. (2004). GO:TermFinder–open source software for accessing Gene Ontology information and finding significantly enriched Gene Ontology terms associated with a list of genes. Bioinformatics *20*, 3710–3715.

Buchan, J.R., Muhlrad, D., and Parker, R. (2008). P bodies promote stress granule assembly in Saccharomyces cerevisiae. J. Cell Biol. *183*, 441–455.

Carmo-Silva, S., Nobrega, C., Pereira de Almeida, L., and Cavadas, C. (2017). Unraveling the Role of Ataxin-2 in Metabolism. Trends Endocrinol. Metab. *28*, 309–318.

Chen, J., Sutter, B.M., Shi, L., and Tu, B.P. (2017). GATOR1 regulates nitrogenic cataplerotic reactions of the mitochondrial TCA cycle. Nat. Chem. Biol. *13*, 1179–1186.

Cox, J., and Mann, M. (2008). MaxQuant enables high peptide identification rates, individualized p.p.b.-range mass accuracies and proteome-wide protein quantification. Nat. Biotechnol *26*, 1367–1372.

Drost, J., Nonis, D., Eich, F., Leske, O., Damrath, E., Brunt, E.R., Lastres-Becker, I., Heumann, R., Nowock, J., and Auburger, G. (2013). Ataxin-2 modulates the levels of Grb2 and SRC but not ras signaling. J. Mol. Neurosci. *51*, 68–81.

Elden, A.C., Kim, H.J., Hart, M.P., Chen-Plotkin, A.S., Johnson, B.S., Fang, X., Armakola, M., Geser, F., Greene, R., Lu, M.M., et al. (2010). Ataxin-2 intermediate-length polyglutamine expansions are associated with increased risk for ALS. Nature *466*, 1069–1075.

Ferrezuelo, F., Colomina, N., Palmisano, A., Garí, E., Gallego, C., Csikász-Nagy, A., and Aldea, M. (2012). The critical size is set at a single-cell level by growth rate to attain homeostasis and adaptation. Nat. Commun. *3*, 1012.

Filer, D., Thompson, M.A., Takhaveev, V., Dobson, A.J., Kotronaki, I., Green, J.W.M., Heinemann, M., Tullet, J.M.A., and Alic, N. (2017). RNA polymerase III limits longevity downstream of TORC1. Nature *552*, 263–267.

Fittschen, M., Lastres-Becker, I., Halbach, M.V., Damrath, E., Gispert, S., Azizov, M., Walter, M., Müller, S., and Auburger, G. (2015). Genetic ablation of ataxin-2 increases several global translation factors in their transcript abundance but decreases translation rate. Neurogenetics *16*, 181–192.

Geddes, A.J., Parker, K.D., Atkins, E.D., and Beighton, E. (1968). "Cross-beta" conformation in proteins. J. Mol. Biol. *32*, 343–358.

Han, T.W., Kato, M., Xie, S., Wu, L.C., Mirzaei, H., Pei, J., Chen, M., Xie, Y., Allen, J., Xiao, G., and McKnight, S.L. (2012). Cell-free formation of RNA granules: bound RNAs identify features and components of cellular assemblies. Cell *149*, 768–779.

Huberts, D.H., Sik Lee, S., Gonzáles, J., Janssens, G.E., Vizcarra, I.A., and Heinemann, M. (2013). Construction and use of a microfluidic dissection platform for long-term imaging of cellular processes in budding yeast. Nat. Protoc. *8*, 1019–1027.

Huberts, D.H., González, J., Lee, S.S., Litsios, A., Hubmann, G., Wit, E.C., and Heinemann, M. (2014). Calorie restriction does not elicit a robust extension of replicative lifespan in Saccharomyces cerevisiae. Proc. Natl. Acad. Sci. USA *111*, 11727–11731.

Janssens, G.E., Meinema, A.C., González, J., Wolters, J.C., Schmidt, A., Guryev, V., Bischoff, R., Wit, E.C., Veenhoff, L.M., and Heinemann, M. (2015). Protein biogenesis machinery is a driver of replicative aging in yeast. eLife *4*, e08527.

Kanki, T., Kang, D., and Klionsky, D.J. (2009). Monitoring mitophagy in yeast: the Om45-GFP processing assay. Autophagy *5*, 1186–1189.

Kato, M., Han, T.W., Xie, S., Shi, K., Du, X., Wu, L.C., Mirzaei, H., Goldsmith, E.J., Longgood, J., Pei, J., et al. (2012). Cell-free formation of RNA granules: low complexity sequence domains form dynamic fibers within hydrogels. Cell *149*, 753–767.

Kato, M., Yang, Y.-S., Sutter, B.M., Wang, Y., McKnight, S.L., and Tu, B.P. (2019). Redox State Controls Phase Separation of the Yeast Ataxin-2 Protein via Reversible Oxidation of its Methionine-Rich Low Complexity Domain. Cell *177*. https://doi.org/10.1016/j.cell.2019.02.044.

Kroschwald, S., Maharana, S., Mateju, D., Malinovska, L., Nüske, E., Poser, I., Richter, D., and Alberti, S. (2015). Promiscuous interactions and protein disaggregases determine the material state of stress-inducible RNP granules. eLife *4*, e06807.

Lastres-Becker, I., Rüb, U., and Auburger, G. (2008). Spinocerebellar ataxia 2 (SCA2). Cerebellum *7*, 115–124.

Laxman, S., Sutter, B.M., Wu, X., Kumar, S., Guo, X., Trudgian, D.C., Mirzaei, H., and Tu, B.P. (2013). Sulfur amino acids regulate translational capacity and metabolic homeostasis through modulation of tRNA thiolation. Cell *154*, 416–429.

Laxman, S., Sutter, B.M., Shi, L., and Tu, B.P. (2014). Npr2 inhibits TORC1 to prevent inappropriate utilization of glutamine for biosynthesis of nitrogen-containing metabolites. Sci. Signal. *7*, ra120.

Lee, S.S., Avalos Vizcarra, I., Huberts, D.H., Lee, L.P., and Heinemann, M. (2012). Whole lifespan microscopic observation of budding yeast aging through a microfluidic dissection platform. Proc. Natl. Acad. Sci. USA *109*, 4916–4920.

Levine, B., and Klionsky, D.J. (2004). Development by self-digestion: molecular mechanisms and biological functions of autophagy. Dev. Cell *6*, 463–477.

Lin, Y., Mori, E., Kato, M., Xiang, S., Wu, L., Kwon, I., and McKnight, S.L. (2016). Toxic PR Poly-Dipeptides Encoded by the C9orf72 Repeat Expansion Target LC Domain Polymers. Cell *167*, 789–802.

Longtine, M.S., McKenzie, A., 3rd, Demarini, D.J., Shah, N.G., Wach, A., Brachat, A., Philippsen, P., and Pringle, J.R. (1998). Additional modules for versatile and economical PCR-based gene deletion and modification in Saccharomyces cerevisiae. Yeast *14*, 953–961.

Mangus, D.A., Amrani, N., and Jacobson, A. (1998). Pbp1p, a factor interacting with Saccharomyces cerevisiae poly(A)-binding protein, regulates polyadenylation. Mol. Cell. Biol. *18*, 7383–7396.

Molliex, A., Temirov, J., Lee, J., Coughlin, M., Kanagaraj, A.P., Kim, H.J., Mittag, T., and Taylor, J.P. (2015). Phase separation by low complexity domains promotes stress granule assembly and drives pathological fibrillization. Cell *163*, 123–133.

Nixon, R.A. (2013). The role of autophagy in neurodegenerative disease. Nat. Med. *19*, 983–997.

Noda, T., Matsuura, A., Wada, Y., and Ohsumi, Y. (1995). Novel system for monitoring autophagy in the yeast Saccharomyces cerevisiae. Biochem. Biophys. Res. Commun. *210*, 126–132.

Nonhoff, U., Ralser, M., Welzel, F., Piccini, I., Balzereit, D., Yaspo, M.L., Lehrach, H., and Krobitsch, S. (2007). Ataxin-2 interacts with the DEAD/H-box RNA helicase DDX6 and interferes with P-bodies and stress granules. Mol. Biol. Cell *18*, 1385–1396.

Otsu, N. (1979). A threshold selection method from gray-level histograms. IEEE Trans. Syst. Man Cybern. *9*, 62–66.

Panchaud, N., Péli-Gulli, M.P., and De Virgilio, C. (2013). Amino acid deprivation inhibits TORC1 through a GTPase-activating protein complex for the Rag family GTPase Gtr1. Sci. Signal. *6*, ra42.

Prouteau, M., Desfosses, A., Sieben, C., Bourgoint, C., Lydia Mozaffari, N., Demurtas, D., Mitra, A.K., Guichard, P., Manley, S., and Loewith, R. (2017). TORC1 organized in inhibited domains (TOROIDs) regulate TORC1 activity. Nature *550*, 265–269.

Ralser, M., Albrecht, M., Nonhoff, U., Lengauer, T., Lehrach, H., and Krobitsch, S. (2005). An integrative approach to gain insights into the cellular function of human ataxin-2. J. Mol. Biol. *346*, 203–214.

Ravikumar, B., Vacher, C., Berger, Z., Davies, J.E., Luo, S., Oroz, L.G., Scaravilli, F., Easton, D.F., Duden, R., O'Kane, C.J., and Rubinsztein, D.C. (2004). Inhibition of mTOR induces autophagy and reduces toxicity of polyglutamine expansions in fly and mouse models of Huntington disease. Nat. Genet. *36*, 585–595.

Ribbeck, K., and Görlich, D. (2002). The permeability barrier of nuclear pore complexes appears to operate via hydrophobic exclusion. EMBO J. *21*, 2664–2671.

Romero, C.M., Paez, M.S., Miranda, J.A., Hernandez, D.J., and Oviedo, L.E. (2007). Effect of temperature on the surface tension of diluted aqueous solutions of 1,2-hexanediol, 1,5-hexanediol, 1,6-hexanediol and 2,5-hexanediol. Fluid Phase Equilib. *258*, 67–72.

Sellier, C., Campanari, M.L., Julie Corbier, C., Gaucherot, A., Kolb-Cheynel, I., Oulad-Abdelghani, M., Ruffenach, F., Page, A., Ciura, S., Kabashi, E., and Charlet-Berguerand, N. (2016). Loss of C9ORF72 impairs autophagy and synergizes with polyQ Ataxin-2 to induce motor neuron dysfunction and cell death. EMBO J. *35*, 1276–1297.

Sheffield, P., Garrard, S., and Derewenda, Z. (1999). Overcoming expression and purification problems of RhoGDI using a family of "parallel" expression vectors. Protein Expr. Purif. *15*, 34–39.

Shi, K.Y., Mori, E., Nizami, Z.F., Lin, Y., Kato, M., Xiang, S., Wu, L.C., Ding, M., Yu, Y., Gall, J.G., and McKnight, S.L. (2017). Toxic PR_n poly-dipeptides encoded by the *C9orf72* repeat expansion block nuclear import and export. Proc. Natl. Acad. Sci. USA *114*, E1111–E1117.

Sunde, M., and Blake, C. (1997). The structure of amyloid fibrils by electron microscopy and X-ray diffraction. Adv. Protein Chem. *50*, 123–159.

Sutter, B.M., Wu, X., Laxman, S., and Tu, B.P. (2013). Methionine inhibits autophagy and promotes growth by inducing the SAM-responsive methylation of PP2A. Cell *154*, 403–415.

Swisher, K.D., and Parker, R. (2010). Localization to, and effects of Pbp1, Pbp4, Lsm12, Dhh1, and Pab1 on stress granules in Saccharomyces cerevisiae. PLoS ONE *5*, e10006.

Takahara, T., and Maeda, T. (2012). Transient sequestration of TORC1 into stress granules during heat stress. Mol. Cell *47*, 242–252.

Tatton, W.G., and Olanow, C.W. (1999). Apoptosis in neurodegenerative diseases: the role of mitochondria. Biochim. Biophys. Acta *1410*, 195–213.

van Dijken, J.P., Bauer, J., Brambilla, L., Duboc, P., Francois, J.M., Gancedo, C., Giuseppin, M.L., Heijnen, J.J., Hoare, M., Lange, H.C., et al. (2000). An interlaboratory comparison of physiological and genetic properties of four Saccharomyces cerevisiae strains. Enzyme Microb. Technol. *26*, 706–714.

Wootton, J.C. (1994). Non-globular domains in protein sequences: automated segmentation using complexity measures. Comput. Chem. *18*, 269–285.

Wu, X., and Tu, B.P. (2011). Selective regulation of autophagy by the Iml1-Npr2-Npr3 complex in the absence of nitrogen starvation. Mol. Biol. Cell *22*, 4124–4133.

Wullschleger, S., Loewith, R., and Hall, M.N. (2006). TOR signaling in growth and metabolism. Cell *124*, 471–484.

Zopf, C.J., Quinn, K., Zeidman, J., and Maheshri, N. (2013). Cell-cycle dependence of transcription dominates noise in gene expression. PLoS Comput. Biol. *9*, e1003161.

STAR★METHODS

KEY RESOURCES TABLE

REAGENT or RESOURCE	SOURCE	IDENTIFIER
Antibodies		
Mouse monoclonal anti-Flag	Sigma	Cat#F1804; RRID: AB_262044
Rabbit anti-FLAG M2 antibody	Cell signaling	Cat#2368; RRID: AB_2217020
Mouse monoclonal Anti-GFP (clone 7.1 and 13.1)	Roche	Cat#11814460001; RRID: AB_390913
Rabbit Anti-HA antibody	Cell signaling	Cat#3724; RRID: AB_1549585
Rabbit Anti-G6PD ab2	Sigma	Cat#A9521; RRID: AB_258454
Chemicals, Peptides, and Recombinant Proteins		
Rapamycin	Calbiochem	Cat#553210
Cycloheximide	Sigma	Cat#C7698
Ribonuclease A	Sigma	Cat#R4642
H_2O_2	Sigma	Cat#216763
Antimycin A	Sigma	Cat#A8674
Dynabeads protein G	Life technologies	Cat#10004D
1,6-hexanediol	Sigma	Cat#240117
2,5-hexanediol	Sigma	Cat#411904
Phos-tag Acrylamide	Wako chemical laboratory	Cat#304-93521
Protease inhibitor cocktail	Roche	Cat#5056489001
p-nitrophenyl phosphate	Life Technologies	Cat#002201
L-Lysine:2HCl (U-13C6,99%; U-15N2,99%)	Cambridge Isotope Laboratories	Cat#CNLM-291-H-0.05
L-Arginine:HCl (U-13C6,99%; U-15N4,99%)	Cambridge Isotope Laboratories	Cat#CNLM-539-H-0.1
Critical Commercial Assays		
BCA protein assay kit	Thermo	Cat#23227
Experimental Models: Organisms/Strains		
Sccharomyces cerevisiae strain CEN.PK: genotype: ho::ADH1^{P}-Mito-dsRed::KanMX, Vph1-GFP::natNT	Wu and Tu, 2011	N/A
S.cerevisiae strain CEN.PK: genotype: ho::ADH1^{P}-Mito-dsRed::KanMX, Vph1-GFP::natNT, pbp1Δ::Hyg	this paper	N/A
S.cerevisiae strain CEN.PK: genotype: Idh1-GFP::KanMX	Wu and Tu, 2011	N/A
S.cerevisiae strain CEN.PK: genotype: Idh1-GFP::KanMX, pbp1Δ::Hyg	this paper	N/A
S.cerevisiae strain CEN.PK: genotype: pho8::TEF1^{P}-pho8Δ60::KanMX, pho13T::natNT	Wu and Tu, 2011	N/A
S.cerevisiae strain CEN.PK: genotype: pho8::TEF1^{P}-pho8Δ60::KanMX, pho13T::natNT, pbp1Δ::Hyg	this paper	N/A
S.cerevisiae strain CEN.PK: genotype: WT	van Dijken et al., 2000	N/A
S.cerevisiae strain CEN.PK: genotype: pbp1Δ::Hyg	this study	N/A
S.cerevisiae strain CEN.PK: genotype: Sch9-3xHA::natNT	Laxman et al., 2014	N/A
S.cerevisiae strain CEN.PK: genotype: Sch9-3xHA::natNT, pbp1Δ::Hyg	this paper	N/A
S.cerevisiae strain CEN.PK: genotype: 3HA-Atg13::natNT	Wu and Tu, 2011	N/A
S.cerevisiae strain CEN.PK: genotype: 3HA-Atg13::natNT, pbp1Δ::Hyg	this paper	N/A
S.cerevisiae strain CEN.PK: genotype: lys1Δ::KanMX, arg1Δ::Hyg	Laxman et al., 2013	N/A
S.cerevisiae strain CEN.PK: genotype: lys1Δ::KanMX, arg1Δ::Hyg, pbp1Δ::natNT	this paper	N/A

(*Continued on next page*)

Continued

REAGENT or RESOURCE	SOURCE	IDENTIFIER
S.cerevisiae strain CEN.PK: genotype: Kog1-3xHA::KanMX	this paper	N/A
S.cerevisiae strain CEN.PK: genotype: Kog1-3xHA::KanMX, Pbp1-3xFlag::Hyg	this paper	N/A
S.cerevisiae strain CEN.PK: genotype: Pbp1-GFP::Hyg	this paper	N/A
S.cerevisiae strain CEN.PK: genotype: Pbp1-3xFlag::Hyg	this paper	N/A
S.cerevisiae strain CEN.PK: genotype: Pbp1-GFP::Hyg, Vph1-mCherry::KanMX	this paper	N/A
S.cerevisiae strain CEN.PK: genotype: Pbp1-GFP::Hyg, Sec63-mCherry::KanMX	this paper	N/A
S.cerevisiae strain CEN.PK: genotype: ho::ADH1^{P}-Mito-dsRed::KanMX, Pbp1-GFP::Hyg	this paper	N/A
S.cerevisiae strain CEN.PK Diploid: genotype: WT/Pbp1-3xHA::KanMX	this paper	N/A
S.cerevisiae strain CEN.PK Diploid: genotype: Pbp1-3xFlag::Hyg/Pbp1-3xHA::KanMX	this paper	N/A
S.cerevisiae strain CEN.PK: genotype: Idh1-GFP::KanMX, pbp1Δ::pbp1Δa.a.50-127-3xFlag::Hyg	this paper	N/A
S.cerevisiae strain CEN.PK: genotype: Idh1-GFP::KanMX, pbp1Δ::pbp1Δa.a.226-298-3xFlag::Hyg	this paper	N/A
S.cerevisiae strain CEN.PK: genotype: Idh1-GFP::KanMX, pbp1Δ::pbp1Δa.a.50-298-3xFlag::Hyg	this paper	N/A
S.cerevisiae strain CEN.PK: genotype: pbp1Δ::pbp1Δa.a.50-127-3xFlag::Hyg	this paper	N/A
S.cerevisiae strain CEN.PK: genotype: pbp1Δ::pbp1Δa.a.226-298-3xFlag::Hyg	this paper	N/A
S.cerevisiae strain CEN.PK: genotype: pbp1Δ::pbp1Δa.a.50-298-3xFlag::Hyg	this paper	N/A
S.cerevisiae strain CEN.PK: genotype: pbp1Δ::pbp1a.a.571-722-GFP::Hyg	this paper	N/A
S.cerevisiae strain CEN.PK: genotype: pbp1Δ::pbp1Δa.a.571-722-3xFlag::Hyg	this paper	N/A
S.cerevisiae strain CEN.PK: genotype: pbp1Δ::pbp1Δa.a.571-722-GFP::Hyg	this paper	N/A
S.cerevisiae strain CEN.PK: genotype: Idh1-GFP::KanMX, pbp1Δ::pbp1Δa.a.571-722-3xFlag::Hyg	this paper	N/A
S.cerevisiae strain CEN.PK: genotype: Idh1-GFP::KanMX, pbp1Δ::pbp1M614,616S-3xFlag::Hyg	this paper	N/A
S.cerevisiae strain CEN.PK: genotype: Idh1-GFP::KanMX, pbp1Δ::pbp1M614,616, 618, 625S-3xFlag::Hyg	this paper	N/A
S.cerevisiae strain CEN.PK: genotype: Idh1-GFP::KanMX, pbp1Δ::pbp1M605, 606, 614,616, 618, 625S-3xFlag::Hyg	this paper	N/A
S.cerevisiae strain CEN.PK: genotype: Idh1-GFP::KanMX, pbp1Δ::pbp1M591, 595, 605, 606, 614,616, 618, 625S-3xFlag::Hyg	this paper	N/A
S.cerevisiae strain CEN.PK: genotype: pbp1Δ::pbp1M614,616S-3xFlag::Hyg	this paper	N/A
S.cerevisiae strain CEN.PK: genotype: pbp1Δ::pbp1M614,616, 618, 625S-3xFlag::Hyg	this paper	N/A
S.cerevisiae strain CEN.PK: genotype: pbp1Δ::pbp1M605, 606, 614, 616, 618, 625S-3xFlag::Hyg	this paper	N/A
S.cerevisiae strain CEN.PK: genotype: pbp1Δ::pbp1M591, 595, 605, 606, 614,616, 618, 625S-3xFlag::Hyg	this paper	N/A
S.cerevisiae strain CEN.PK: genotype: atg1Δ::KanMX	Wu and Tu, 2011	N/A
S.cerevisiae strain CEN.PK: genotype: Gln3-3xFlag::natNT	this paper	N/A

(*Continued on next page*)

Continued

REAGENT or RESOURCE	SOURCE	IDENTIFIER
S.cerevisiae strain CEN.PK: genotype: Gln3-3xFlag::natNT, pbp1Δ::Hyg	this paper	N/A
S.cerevisiae strain CEN.PK: genotype: Npr1-3xFlag::natNT	this paper	N/A
S.cerevisiae strain CEN.PK: genotype: Npr1-3xFlag::natNT, pbp1Δ::Hyg	this paper	N/A
S.cerevisiae strain CEN.PK: genotype: Kog1-superfolderGFP::KanMX	this paper	N/A
S.cerevisiae strain CEN.PK: genotype: Kog1-superfolderGFP::KanMX, pbp1Δ::Hyg	this paper	N/A
S.cerevisiae strain CEN.PK: genotype: Pab1-mCherry::KanMX	this paper	N/A
S.cerevisiae strain CEN.PK: genotype: Pub1-mCherry::KanMX	this paper	N/A
S.cerevisiae strain CEN.PK: genotype: Pbp1-3xHA::KanMX	this paper	N/A
S.cerevisiae strain CEN.PK: genotype: Kog1-3xHA::KanMX, pbp1Δ::pbp1Δa.a.50-127-3xFlag::Hyg	this paper	N/A
S.cerevisiae strain CEN.PK: genotype: Kog1-3xHA::KanMX, pbp1Δ::pbp1Δa.a.226-298-3xFlag::Hyg	this paper	N/A
S.cerevisiae strain CEN.PK: genotype: Kog1-3xHA::KanMX, pbp1Δ::pbp1Δa.a.50-298-3xFlag::Hyg	this paper	N/A
S.cerevisiae strain CEN.PK: genotype: Kog1-3xHA::KanMX, pbp1Δ::pbp1Δa.a.571-722-3xFlag::Hyg	this paper	N/A
S.cerevisiae strain CEN.PK: genotype: Kog1-3xHA::KanMX, pbp1Δ::pbp1Δa.a.2-49-3xFlag::Hyg	this paper	N/A
S.cerevisiae strain CEN.PK: genotype: Kog1-3xHA::KanMX, pbp1Δ::pbp1Δa.a.299-570-3xFlag::Hyg	this paper	N/A
S.cerevisiae strain CEN.PK: genotype: Kog1-3xHA::KanMX, pbp1Δ::pbp1Δa.a.299-420-3xFlag::Hyg	this paper	N/A
S.cerevisiae strain CEN.PK: genotype: Kog1-3xHA::KanMX, pbp1Δ::pbp1Δa.a.421-490-3xFlag::Hyg	this paper	N/A
S.cerevisiae strain CEN.PK: genotype: Kog1-3xHA::KanMX, pbp1Δ::pbp1Δa.a.491-570-3xFlag::Hyg	this paper	N/A
S.cerevisiae strain CEN.PK: genotype: Kog1-3xHA::KanMX, pbp1Δ::pbp1Δa.a.299-337-3xFlag::Hyg	this paper	N/A
S.cerevisiae strain CEN.PK: genotype: Kog1-3xHA::KanMX, pbp1Δ::pbp1Δa.a.338-387-3xFlag::Hyg	this paper	N/A
S.cerevisiae strain CEN.PK: genotype: Kog1-3xHA::KanMX, pbp1Δ::pbp1Δa.a.388-442-3xFlag::Hyg	this paper	N/A
S.cerevisiae strain CEN.PK: genotype: Kog1-3xHA::KanMX, pbp1Δ::pbp1Δa.a.443-490-3xFlag::Hyg	this paper	N/A
S.cerevisiae strain CEN.PK: genotype: pbp1Δ::pbp1Δa.a.338-387-3xFlag::Hyg	this paper	N/A
S.cerevisiae strain CEN.PK: genotype: pbp1Δ::pbp1Δa.a.388-442-3xFlag::Hyg	this paper	N/A
S.cerevisiae strain CEN.PK: genotype: Idh1-GFP::KanMX, pbp1Δ::pbp1Δa.a.338-387-3xFlag::Hyg	this paper	N/A
S.cerevisiae strain CEN.PK: genotype: Idh1-GFP::KanMX, pbp1Δ::pbp1Δa.a.388-442-3xFlag::Hyg	this paper	N/A
S.cerevisiae strain CEN.PK: genotype: Pbp1-yoEGFP::KanMX	Kato et al., 2019	N/A
Recombinant DNA		
Plasmid: 6xHis-Pbp1aa570-722 in pET28 backbone pHis.Parallel1 background	this paper	N/A
Plasmid: 6xHis-GFP-Pbp1aa570-722 in pHis.Parallel1 background	this paper	N/A
Plasmid: 6xHis-Pbp1aa570-722 M614,616S in pHis.Parallel1 backbone	this paper	N/A
Plasmid: 6xHis-Pbp1aa570-722 M614,616, 618, 625S in pHis.Parallel1 backbone	this paper	N/A

(*Continued on next page*)

Continued

REAGENT or RESOURCE	SOURCE	IDENTIFIER
Plasmid: 6xHis-Pbp1aa570-722 M605, 606, 614,616, 618, 625 in pHis.Parallel1 backbone	this paper	N/A
Plasmid: 6xHis-Pbp1aa570-722 M591, 595, 605, 606, 614,616, 618, 625S in pHis.Parallel1 backbone	this paper	N/A
Plasmid: 6xHis-GFP-Pbp1aa570-722 M591, 595, 605, 606, 614,616, 618, 625S in pHis.Parallel1 backbone	this paper	N/A
Software and Algorithms		
ImageJ	NIH	https://imagej.nih.gov/ij/
Prism	Graphpad software	https://www.graphpad.com/
MATLAB	Mathworks	https://www.mathworks.com/
Code for methionine content analysis	this paper	https://github.com/tulabutsw/methionine-content-analysis-
Code for image analysis	this paper	https://github.com/tulabutsw/image_analysis

CONTACT FOR REAGENT AND RESOURCE SHARING

Further information and requests for resources and reagents should be directed to and will be fulfilled by the Lead Contact, Benjamin Tu (benjamin.tu@utsouthwestern.edu)

EXPERIMENTAL MODEL AND SUBJECT DETAILS

Yeast strains

The prototrophic *Saccharomyces cerevisiae* CEN.PK strain (van Dijken et al., 2000) was used in all experiments. All strains used in this study are listed in the KEY RESOURCES TABLE. Gene deletions were carried out using standard PCR-based strategies to amplify resistance cassettes with appropriate flanking sequences, and replacing the target gene by homologous recombination (Longtine et al., 1998). C-terminal tags were similarly made using PCR to amplify resistance cassettes with flanking sequences. The diploid strain was constructed by standard mating procedures. Pbp1 mutants with various domain deletion or point mutations were first made using PCR and then integrated into the *PBP1* locus in a *pbp1Δ* strain with different selection markers.

Yeast growth media and procedures

Media used in this study

YPL (0.5% yeast extract (Bio Basic), 2% peptone (BD Biosciences) and 2% lactate (Sigma L1375)); SL (0.17% yeast nitrogen base without amino acids (BD Biosciences), 2% lactate); SD (0.17% yeast nitrogen base without amino acids, 2% glucose); SD-N (0.17% yeast nitrogen base without amino acids and ammonium sulfate (BD Biosciences), 2% glucose); SCL-Lys-Arg (0.17% yeast nitrogen base without amino acids, CSM-Lys-Arg (Sunrise science), 2% lactate).

Media switch

Cells from overnight YPL culture were inoculated into fresh YPL to 0.1 optical density (OD_{600})/ml and grown for a few generations in log phase. The log-phase cells were then diluted again to very low OD_{600}, grown overnight till the OD_{600} reached ~1. The cells were then spun down, washed, and re-suspended to OD_{600} = 0.7 in SL, SD or SD-N. Samples were collected at indicated times. Growth curves for different cells grown in SL, SD, or SD-N were performed by starting cultures at OD_{600} ~0.15, and then measuring OD_{600} periodically until saturation.

METHOD DETAILS

Assays to monitor autophagy

Imaging

A dual-color reporter strain expressing mitochondrial-localized DsRed (Mito-DsRed) and GFP-tagged vacuolar membrane protein Vph1 (Vph1-GFP) was constructed to visualize mitophagy. An increase in the signal of Mito-DsRed in the vacuole indicates the induction of mitophagy. Images were taken under a 100X oil-immersion objective lens with a Deltavision DVRT microscope. Cells grown under indicated conditions were visualized after directly mounting under a coverslip. Images were deconvolved, then processed using ImageJ.

GFP cleavage assay

A mitochondrial matrix protein, Idh1, was tagged with GFP. When mitophagy is induced, this protein accumulates in the vacuole and is degraded. The more stable GFP is detected by immunoblotting with anti-GFP monoclonal antibody (Roche, clone 7.1 and 13.1) as semiquantitative evidence for mitophagy (Kanki et al., 2009).

ALP activity assay

pho8Δ60/pho13Δ cells with or without Pbp1 were subject to ALP activity assay before and 8 h after media switch to measure the level of general autophagy. The protocol for ALP assay essentially followed previously described methods (Noda et al., 1995) with some modifications. Briefly, cell pellets were resuspended in 400 μL of lysis buffer (250 mM Tris-HCl pH 9, 25 mM $MgSO_4$, 1% Triton, 2X EDTA-free protease inhibitor cocktail (Roche). After adding ~100 μL of glass beads (Sigma), cells were lysed by three rounds of bead beating: 1 min of beating, then 1 min of cooling on ice. Cell debris and glass beads were separated from the cell extracts by centrifugation at maximum speed for 10 min at 4°C. For each sample, 70 μL of cell extracts were added to triplicate wells in 96-well, flat bottom plates. Plates were kept on ice before the substrate was added. Lysis buffer (70 μl) was added to the blank well. 70 μL of substrate solution (250 mM Tris-HCl pH 9, 25 mM $MgSO_4$, 1% Triton, 2.7 mM *p*-nitrophenyl phosphate (MP Biomedicals Life Sciences)) was then added to each well. The plate was incubated at room temperature for 5 min before the reaction was stopped with 140 μL of stop buffer (1 M glycine, pH 11). The plate was read at 400 nm to measure the production of *p*-nitrophenol.

TCA-precipitated whole cell extracts preparation

Cell pellets were resuspended in 250 μL 8% TCA. After adding ~100 μL glass beads, cells were lysed by five rounds of bead-beating: 30 s beating/30 s cooling on ice. The lysates were then centrifuged at maximum speed for 10 min at 4°C. The pellets were then washed with 100% ice-cold acetone and resuspended in 2X SDS sample buffer (400 mM Tris-HCl pH 7.5, 4% SDS, 20% glycerol), boiled for 5 min, and briefly centrifuged. The supernatant was then separated and the protein concentration was measured using BCA protein assay kit (Thermo Scientific). Bromophenol blue and 2-mercaptoethanol were added to the lysates after concentration measurement.

TORC1 substrate phosphorylation

At the indicated time points, 5 OD of cells expressing Sch9-HA, HA-Atg13, Gln3-Flag, or Npr1-Flag were quenched by mixing with TCA to a final concentration of 10% and incubated on ice for 20 min before centrifugation. Cell pellets were then subject to whole cell TCA extraction and analyzed by Western immunoblotting. Sch9-HA samples were analyzed by phos-tag SDS-PAGE (Wako chemical laboratory) immunoblot with anti-HA antibody (Cell Signaling, C29F4). HA-Atg13, Gln3-Flag, or Npr1-Flag samples were analyzed by SDS-PAGE immunoblot with anti-HA and anti-Flag (Sigma, M2) antibodies, respectively. The loading control was immunoblotted with rabbit anti-G6PD Ab2 (Sigma). For cells treated with rapamycin and cycloheximide, 200 ng/ml rapamycin (Sigma) or 25 μg/ml cycloheximide (Sigma) was added to cells grown in YPL and grown for 30 min before harvesting.

SILAC experiments to identify changes in protein abundance

Culture preparation

WT or *pbp1Δ* strains auxotrophic for lysine and arginine (*lys1Δ/arg4Δ*) were grown in YPL for several generations and then diluted to OD_{600} 0.01 in SCL-Lys-Arg media supplemented with 50 μg/ml lysine and 50 μg/ml arginine (Lys^0+Arg^0 for *pbp1Δ* cells, Lys^{+8}+Arg^{+10} for WT cells). For efficient labeling, cells were grown for ~22 h (7-8 complete generations) until OD_{600} ~1. 20 OD of cells at this point were collected as SCL samples and the rest of cultures were washed with SL and resuspended to OD_{600} = 0.7 in SL supplemented with 50 μg/ml lysine and 50 μg/ml arginine (Lys^0+Arg^0 for *pbp1Δ* cells, Lys^{+8}+Arg^{+10} for WT cells). SL samples were collected after 6 h.

Protein Extraction

Cell pellets from WT cells grown in heavy SILAC media were lysed (lysis buffer: 50 mM Tris-HCl pH 8.0, 75 mM NaCl, 50 mM NaF, 50 mM B-glycerophosphate, 1 mM sodium orthovanadate, 5 mM EDTA, 8 M urea, lysis procedures as described earlier for TCA extraction), mixed in 1:1 ratio with *pbp1Δ* cell lysates grown in light media. Proteins in the mixed lysates were separated by SDS-PAGE and stained with Coomassie Blue. Excised gel bands were chopped into 1 mm^3 cubes for in-gel digestion.

In-gel digestion

Coomassie blue stain was removed from gel pieces by incubating for 30 min at 37°C in 50 mM triethylammonium bicarbonate (TEAB)/acetonitrile (1:1, v/v). Gel pieces were then dehydrated with acetonitrile at room temperature, followed by reduction/alkylation using DTT and iodoacetamide. Gel pieces were dehydrated by ACN and rehydrated by a 10 μg/mL solution of trypsin in 0.05% HOAc. The digestion was carried out at 37°C overnight. Peptides were extracted at 37°C for 15 min using the extraction buffer (50% acetonitrile and 3.3% TFA). All the steps above were carried out on a thermomixer shaker (Eppendorf) unless stated otherwise. Extracts were then dried using a speed vacuum concentrator and re-suspended in 2% ACN, 0.1% TFA. Salts were removed using Oasis HLB μElution plate (Waters) before LC-MS/MS analysis.

LC-MS/MS detection of peptides

Reverse phase chromatography was performed on an Ultimate 3000 nano HPLC system (Dionex), equipped with a 75 μm i.d. x 50 cm EasySpray column (Thermo). Separation of peptides was carried out at 250 nl/min by a 60min linear gradient of 1%–28%

buffer B. Buffer A contained 2% (v/v) ACN and 0.1% formic acid in water, and buffer B contained 80% (v/v) ACN, 10% (v/v) trifluoroethanol, and 0.1% formic acid in water.

Mass spectrometric analyses were performed on an Orbitrap Elite Instrument (Thermo Electron). The mass spectrometer operated in positive ion mode with a source voltage of 2.4 kV and a capillary temperature of 255°C. MS scans were acquired at 240,000 resolution in the Orbitrap and up to 14 MS/MS spectra were obtained for each full spectrum acquired using collisionally-induced dissociation (CID) for ions with charges 2 or higher. The charge exclusion was applied to exclude the unassigned and charge 1 species, and dynamic exclusion was used with a duration of 15 s.

SILAC data analysis

RAW data files were analyzed using MaxQuant (version 1.5.0.30) (Cox and Mann, 2008). Peptide and protein identification were performed against the UniProtKB yeast whole proteome sequence database. Default parameters were used for the MaxQuant analysis, with the exception that Ile-leu equivalence was disabled to ensure reported peptide and protein sequences were identical to those in the original sequence database. Precursor mass tolerances were automatically determined by MaxQuant during processing, while MS/MS mass tolerance was 20 ppm. Peptide and protein identifications were filtered to a 1% false discovery rate (FDR). Quantitation of a protein required the presence of at least two quantified peptide features for that protein.

GO term analysis

Proteins with expression level highly increased in *pbp1Δ* cells in SL ($0.5 < (pbp1\Delta/\mathrm{WT})_{SCL} < 1.5$, $(pbp1\Delta/\mathrm{WT})_{SL} > 2$) were analyzed for GO enrichments for biological processes using the GO term finder interface on the *Saccharomyces* Genome Database, including a p value cutoff for significant shared GO terms of 0.01 (Ashburner et al., 2000; Boyle et al., 2004).

Immunoprecipitation

At the indicated time points, 50 OD of cells were harvested, flash frozen with liquid nitrogen, and stored at −80°C until cell lysis. The cell pellet was resuspended with 350 μL of lysis buffer A (50 mM HEPES pH 7.5, 150 mM NaCl, 10 mM $MgCl_2$, 0.5% NP-40, 2X protease inhibitor cocktail, 1 mM PMSF, 1 mM sodium orthovanadate, 5 mM NaF, 10 nM leupeptin, 5 nM pepstatin A). After adding ~300 μL of glass beads, cells were lysed by bead beating 6 times: 30 s of beating / 2 min of cooling on ice. The lysed cells were then separated from glass beads by centrifugation at 6000 rpm for 2 min at 4°C, and diluted with 525 μL of lysis buffer B devoid of NP-40 (50 mM HEPES pH 7.5, 150 mM NaCl, 10 mM $MgCl_2$, 2X protease inhibitor cocktail, 1 mM PMSF, 1 mM sodium orthovanadate, 5 mM NaF, 10 nM leupeptin, 5 nM pepstatin A). The crude cell extracts were then clarified by two successive centrifugations at maximum speed for 10 min at 4°C (Panchaud et al., 2013).

The protein concentration of the cleared lysates was then measured using Bradford assay (Bio-Rad), and adjusted to be equal among all samples in 800 μL reaction volume. For input samples, 8 μL of the reactions were taken and mixed with SDS sample dye, and denatured for 5 min at 95°C. For each co-immunoprecipitation reaction, 25 μL of dynabeads protein G (Life technologies) were washed with the IP lysis buffer and incubated with 3 μg of anti-Flag antibody (Sigma, M2) for 1 h at 4°C. The unbound antibodies were then removed by centrifugation at 500 g for 1 min at 4°, and the conjugated dynabeads-antibody were then added to the cleared lysates. If indicated, ribonuclease A (Sigma) was added to the lysates. After incubating for 2 h at 4°C, the dynabeads were washed 3 times with wash buffer (50 mM HEPES pH 7.5, 150 mM NaCl, 10 mM $MgCl_2$, 2X protease inhibitor cocktail, 0.2% NP-40), resuspended in 2X SDS sample dye, and denatured for 5 min at 95°C.

Fractionation to assess intracellular assembly formation

At the indicated time points, 20 OD of cells were harvested, flash frozen with liquid nitrogen, and stored at −80°C until cell lysis. The cell pellet was resuspended with 250 μL of lysis buffer (150 mM HEPES pH 7.5, 150 mM NaCl, 1 mM EDTA, 0.2% NP-40, 2X protease inhibitor cocktail, 1 mM PMSF, 1 mM DTT). After adding ~100 μL of glass beads, cells were lysed by bead beating 4 times: 30 s of beating / 30 s of cooling on ice. Cell lysates were clarified by centrifugation at 650 g for 2 min at 4°C. For total protein sample, 100 μL of lysates were taken, mixed with SDS sample dye and boiled for 5 min at 95°C. For soluble and pellet samples, 100 μL of lysates were centrifuged at 100,000 g for 1 h at 4°C. The supernatant was transferred to another tube and the pellet was resuspended with 100 μL of 0.2% NP-40 lysis buffer. SDS sample dye was then added to both soluble and pellet samples and boiled for 5 min at 95°C.

Protein expression and purification

All Pbp1 fragments were amplified using PCR from yeast cDNA library and cloned into the multiple cloning sites of the pHis-parallel1 vector (Sheffield et al., 1999). Methionine to serine mutations in the Pbp1 C-terminal LC region were introduced by quickchange site-directed mutagenesis technique and confirmed by sequencing. All proteins were overexpressed in *E. coli* BL21(DE3) cells with 0.5 mM IPTG at 20°C overnight. Harvested cells were lysed with 0.2 mg/ml lysozyme in a lysis buffer containing 50 mM Tris-HCl pH 7.5, 500 mM NaCl, 20 mM 2-mercaptoethanol, 1% Triton X-100, 2 M guanidine hydrochloride and a protein inhibitor tablet (Sigma) for 30 min on ice, and then sonicated for 2 min (10 s on / 30 s off). The cell lysate was centrifuged at 35,000 rpm for 1 h. The supernatant was mixed with Ni-NTA resin (QIAGEN) for 30 min at 4°C. The Ni-NTA resin was packed in a glass column and washed with a washing buffer containing 20 mM Tris-HCl pH 7.5, 500 mM NaCl, 20 mM imidazole, 20 mM 2-mercaptoethanol, 0.1 mM PMSF and 2 M guanidine hydrochloride. The bound proteins were eluted from the resin with a elution buffer containing 20 mM Tris-HCl (pH 7.5), 500 mM NaCl, 200 mM imidazole, 20 mM 2-mercaptoethanol, 0.1 mM PMSF and 2 M guanidine hydrochloride. EDTA was added to a final concentration of 0.5 mM to the eluted protein solutions. The purified proteins were concentrated with Amicon Ultra centrifugal

filters (Millipore) to the final concentration of 100-120 mg/ml. The protein solutions were stored at −80°C. The purities of the purified proteins were confirmed by SDS-PAGE, and the concentrations were determined by absorbance at UV_{280}.

Phase-separated droplet formation

Phase-separated droplets of His_6-Pbp1_LC were formed by a quick dilution of the purified protein (90 mg/ml in 6 M guanidine HCl) into a gelation buffer containing 20 mM Tris-HCl (pH 7.5), 200 mM NaCl, 20 mM 2-mercaptoethanol, 0.1 mM PMSF and 0.5 mM EDTA to reach the final protein concentration of 1-2 mg/ml. The phase-separated droplet solution was incubated for 30 min to 24 h at room temperature. Images of the droplets were taken using Bio-Rad ZOE Fluorescent Cell Imager with a white light mode.

Transmission electron microscopy

To inspect fibril formation, the purified GFP-Pbp1_LC (200-300 μM) were dialyzed in a gelation buffer for overnight. The dialyzed protein solution was deposited on a surface of a TEM grid (CF-400-Cu from Electron Microscopy Sciences, USA). The surface of the grid was washed three times with 10 μL of distilled water. The grid was subsequently stained for 10 s with a 5 μL drop of 2% uranyl acetate. After the uranylacetate solution was blotted, the grid was dried in air. TEM images were obtained with a JEOL 1200EX electron microscope at 120 kV.

X-Ray diffraction

For fibril X-ray diffraction, His_6-Pbp1_LC was diluted in a gelation buffer at 2 mg/ml. The mixture was incubated for 3 days at 4°C. Polymer pellets were collected by centrifuge at 4000 x g for 30 min. The pellets were resuspended in 0.2 mL milli-Q water and dialyzed in 1 L milli-Q water for 12 h twice. The dialyzed samples were lyophilized for overnight and then exposed to an X-ray beam to obtain cross-β diffraction as described previously (Kato et al., 2012).

Dissolution of phase-separated droplets

Dissolution of phase-separated droplets or fibrils of Pbp1_LC by aliphatic alcohols was monitored by turbidity measurements (absorbance at 395 nm wavelength) with Beckman DU800 spectrophotometer. His_6-Pbp1_LC were diluted in the gelation buffer to obtain a final protein concentration of 2 mg/ml (~100 μM). The phase-separated droplet solution (0.5 ml) was dispensed in plastic cuvettes. 1.6-HD or 2,5-HD (50% w/v in gelation buffer) was added to the cuvettes to obtain the indicated concentrations and then incubated at room temperature. The OD_{395} was measured with Beckman DU800 spectrophotometer after 2 min incubation. Plots were calculated from 3 independent experiments.

Semi-denaturing detergent agarose gel electrophoresis (SDD-AGE)

The stability of cross-β polymers were tested by semi-denaturing detergent agarose gel electrophoresis (SDD-AGE) as described previously (Kato et al., 2012). Briefly, the polymers made from His_6-tag Pbp1_LC and the amyloid polymers of yeast Sup35NM protein were diluted in a gelation buffer at 0.2 mg/ml and 0.1 mg/ml, respectively, then sonicated briefly to make the polymers short. The short polymers were incubated in the gelation buffer containing indicated concentrations of SDS (0 - 2%) at 37°C for 10 min. The reaction mixtures were loaded onto 1.5% agarose gel to separate polymers and monomers. Proteins were transferred onto a cellulose membrane and analyzed by western blotting with a His-tag antibody.

Dissolution of phase-separated droplets by dilution

Phase-separated droplets of the WT or the indicated mutants of His_6-Pbp1_LC were formed as described above (2 mg/ml protein concentration). After 30 min incubation at room temperature, the phase-separated droplet solution was dispensed into a 96-well plate and mixed with different volumes of the droplet formation buffer to dilute the protein to the indicated protein concentrations (0 – 2 mg/ml in a total of 100 μl). The plate was incubated at room temperature for 5 min and turbidity of the phase-separated droplet solution was measured at 600 nm using a BIOTEK Cytation5 plate reader. All the samples were measured in triplicate.

Fluorescence recovery after photobleaching (FRAP) and quantification

To make fluorescentally-labeled phase-separated droplets, GFP-Pbp1_LC was first diluted in a gelation buffer at a final concentration of 1 μM. Immediately, His_6-Pbp1_LC was diluted into this solution at a final concentration of 2 mg/ml (~100 μM). The phase-separated droplet solution was dispensed in a glass-bottom microscope dish and incubated at room temperature for 30 min. GFP labeled phase-separated droplets were visualized by confocal microscope (Zeiss LSM880 Airyscan). Time lapse images were recorded with a 5 s interval for a total of 63 images. Photobleaching of GFP signals in selected droplets was carried out after the 3rd image was recorded. GFP intensities of photobleached areas were measured for all the images using ImageJ. The intensities from individual images were normalized against those from the initial image. Plots were generated and curve-fitted using Prism 7 program.

In vivo FRAP experiments were carried out on an Andor Revolution spinning disk confocal microscope with a Nikon 100x oil objective. The 488 nm laser line was used to photobleach a small region of a yeast cell containing one or more discrete GFP puncta. Time lapse images were acquired at 100 nm intervals for three frames before and 1 to 10 s after the bleach using an Ixon Ultra EMCCD (Andor). The Pbp1-yoEGFP strain was described in Kato et al. (2019).

Petite formation

Cells were grown in YPL and then switched to SL as described in Experimental Model and Subject Details. Cell growth in SL was constantly measured to monitor entry into stationary phase. After reaching stationary phase, ~350 cells were plated onto YPD plate at indicated time points, and grown at 30°C for 50 h.

Time-lapse microscopy

For time-lapse microscopy, a microfluidics device (Huberts et al., 2013; Lee et al., 2012) in combination with an inverted fluorescence microscope (Eclipse Ti-E; Nikon instruments, Amsterdam, the Netherlands), an iXon Ultra 897 camera (Andor Technology Ltd, Belfast, United Kingdom), and an LED-based excitation system (AURA light engine; Lumencor, Oregon, USA) were used. For every experiment, exponentially growing cells in SL medium were loaded onto the microfluidics device and were thereafter continuously supplemented with fresh SL medium. Temperature was retained constant at 30° throughout the experiment using a microscope incubator (Life Imaging Services GmbH, 448 Basel, Switzerland). Automated hardware (PFS; Nikon instruments) was used for correction of axial focus fluctuations during time-lapse imaging.

GFP images were taken every 60 min for ≈115 h with excitation at 485 nm (3% LED intensity / 100 msec exposure) using a 470/40 nm bandpass filter, a 495 nm beam-splitter a 525/50 nm emission filter, and a CFI Plan Apochromat Lambda 60X objective (Nikon instruments). Bright field images were recorded every 10 minutes.

Image processing

The cell cytoplasm was determined through global intensity thresholding using Otsu's method (Otsu, 1979). Briefly, OTSU's method divides the pixel intensities into two classes by finding an optimum threshold that minimizes the within-class variance or, equivalently, maximizes the between-class variance (Otsu, 1979). Using this optimum threshold the images were divided into foreground, i.e., cell cytoplasm, and background. Next, connected components smaller than 25 pixels were removed and small holes in the foreground, if any, were filled using morphological closure with a 5-by-5 square-structuring element. Next, we calculated the mean and the standard deviation of the pixel intensities on the foreground. The image analysis was implemented in MATLAB 2018a. Specifically, Otsu's method was implemented using imbinarize function and morphological closing was implemented using imclose function. The code and two example images are available at https://github.com/tulabutsw/image_analysis

Cell division period and replicative lifespan assays

For cell segmentation and fluorescence measurements, the semi-automated ImageJ plugin BudJ was used (Ferrezuelo et al., 2012). Fluorescent measurements were corrected for background fluorescence using the modal fluorescence value provided by BudJ for GFP. The number of buds produced by individual cells and the timing of the onset of budding and cell death were recorded manually by visual inspection of the 60X bright field images, and data were analyzed as described previously (Filer et al., 2017; Huberts et al., 2014) to estimate the RLS. Division periods were determined by estimating the time between two subsequent budding events. G1 duration of daughter cells was determined as the time between cytokinesis (indicated by the darkening of the bud neck in bright field images (Zopf et al., 2013) and the subsequent displacement of the daughter cell away from the mother cell) and bud appearance. The duration of replicative senescence was estimated by calculating the time between last budding event and cell death as indicated by the shrinkage of the cell body. Plotting and statistical analysis were performed using GraphPad Prism and Python.

Identification and quantification of cells with abnormal morphology

For characterization of terminal morphology, bright-filed images of cells that were tracked until cell-death were analyzed (n = 32 for *pbp1Δ* and n = 43 for WT). Abnormal cellular morphology was identified by the presence of multiple interconnected and/or overly elongated buds attached to the cell body at the moment of cell death.

Proteome-wide analysis of methionine content

To estimate the significance of the enrichment of methionine in the C-terminal low complexity region (150 aa) of Pbp1, we counted the number of methionines in all possible windows of 150 amino acids of all protein sequences in the genome of *S. cerevisiae*. A total of 5917 protein sequences obtained from the *Saccharomyces* Genome Database were analyzed: (https://downloads.yeastgenome.org/sequence/S288C_reference/orf_protein/orf_trans.fasta.gz, 13-Jan-2015 12:21). Each protein sequence was analyzed using a sliding window of a length of 150 amino acids. Therefore, a given protein sequence of X amino acids will give (X–150+1) windows. Proteins that are shorter than 150 amino acids were treated as one window. The number of methionines in each window was counted, which serves as the null distribution of methionine enrichment. The significance (p value) of the observed methionine enrichment of in the C-terminal low complexity region of Pbp1 was evaluated by the percentage of windows in the null distribution that contains more methionine than the observed one in the C-terminal low complexity region of Pbp1. All analysis was done using an in-house MATLAB script available at: https://github.com/tulabutsw/methionine-content-analysis-.

QUANTIFICATION AND STATISTICAL ANALYSIS

Low complexity sequence analysis

LC sequences were identified using the SEG program with default parameter settings available at http://mendel.imp.ac.at/METHODS/seg.server.html (Wootton, 1994).

DATA AND SOFTWARE AVAILABILITY

Methionine content analysis

MATLAB script available at: https://github.com/tulabutsw/methionine-content-analysis-

Image processing analysis

The code and two example images are available at: https://github.com/tulabutsw/image_analysis

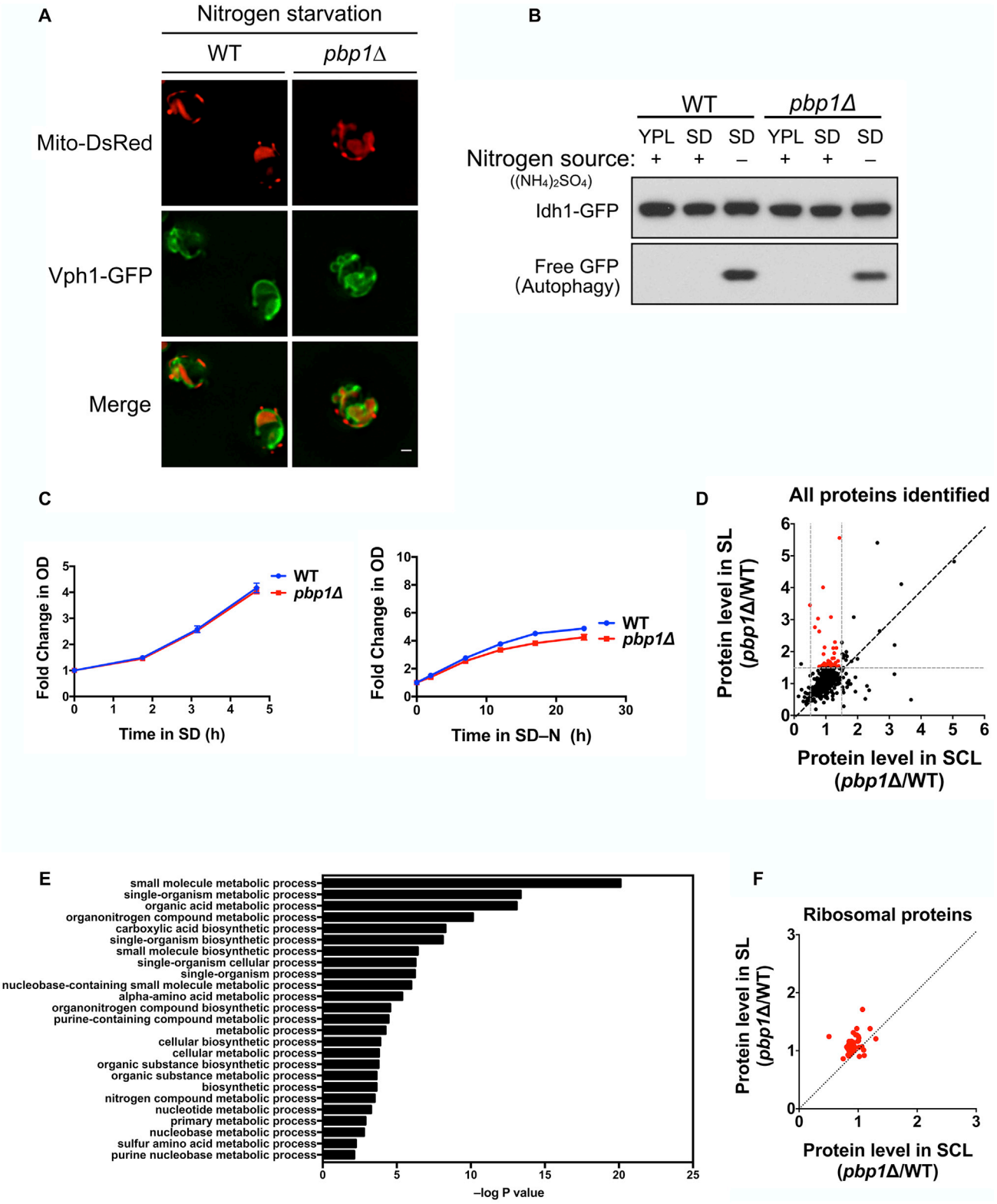

Figure S1. Pbp1 Is a Negative Regulator of TORC1 that Functions during Respiratory Growth, Related to Figure 1

(A) Images of WT and *pbp1Δ* cells after switching from YPL to SD–N medium for 8 h. *pbp1Δ* mutant cells were able to induce mitophagy following switch to SD-N medium. Scale bar = 1 μm.

(legend continued on next page)

(B) GFP cleavage assay showing *pbp1Δ* cells were able to induce mitophagy following switch to SD-N.
(C) Growth of WT and *pbp1Δ* cells in SD and SD–N medium. *pbp1Δ* cells exhibited comparable cell growth to WT in the presence of glucose. Data were mean ± SD from 3 independent experiments.
(D) SILAC quantitative proteomic approach for assessing global changes in protein levels in *pbp1Δ* versus WT cells. The ratios of the expression amounts of all 608 proteins detected in *pbp1Δ* versus WT cells were plotted. Proteins present at increased amounts in *pbp1Δ* in SL ($(pbp1\Delta / WT)_{SL} > 1.5$), but not in SCL ($0.5 < (pbp1\Delta / WT)_{SCL} < 1.5$) are highlighted in red, and listed in Table S1.
(E) Gene ontology analysis for proteins that exhibit increased abundance in *pbp1Δ* cells in SL medium (proteins highlighted in red in (D)).
(F) Correlation plot comparing the amounts of ribosomal proteins in *pbp1Δ* versus WT cells in SCL (x axis) and SL (y axis). Ribosomal proteins were increased in abundance in *pbp1Δ* cells in SL medium. Protein identities are listed in Table S2.

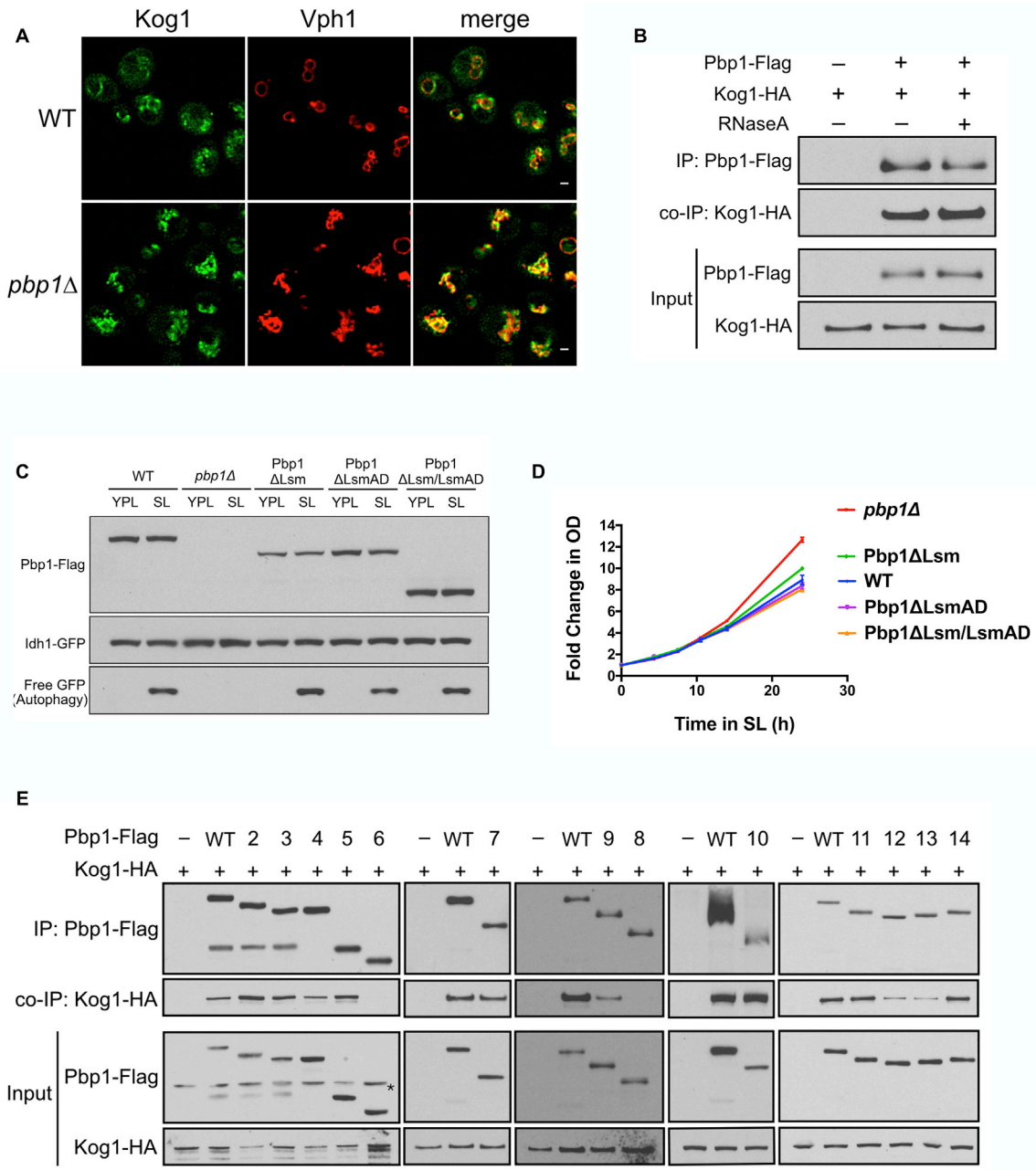

Figure S2. Regions of the Pbp1 Protein Required for Interaction and Inhibition of TORC1, Related to Figure 2

(A) Images of Kog1-superfolderGFP expressed at endogenous levels in WT and *pbp1Δ* cells in SL medium. Vph1: vacuolar membrane protein. Scale bar = 1 μm.

(B) RNase A treatment did not affect the interaction between Kog1 and Pbp1. 200 μg/ml RNase A was added to cell lysates before immunoprecipitation of Pbp1.

(C) GFP cleavage assay showing autophagy in cells expressing Pbp1 mutants lacking the putative RNA-binding domains alone or in combination. Deletion of these domains did not affect autophagy.

(D) Growth curves of cells expressing the indicated variants of Pbp1. Data were mean ± SD from 3 independent experiments.

(E) Immunoprecipitation assessing the interaction between Kog1 and various Pbp1 deletion mutants shown in Figure 2C. Cell culture and immunoprecipitation were performed as described in Figure 2A. Note that the Pbp1 mutants lacking aa338-442 (mutant 6, 8, 9, 12, 13) showed reduced interaction with Kog1. *non-specific signal

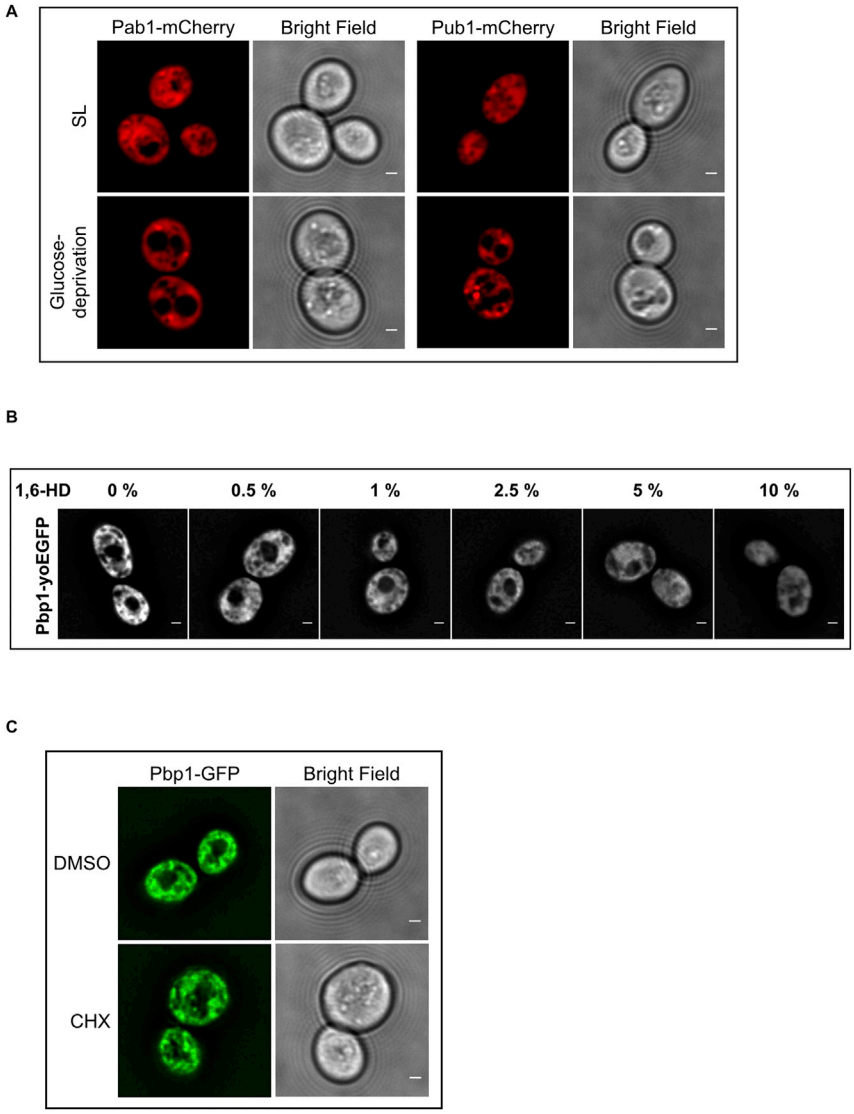

Figure S3. Pbp1 and Other Stress Granule-Associated Proteins Do Not Form Foci-like Granules When Expressed at Endogenous Levels during Respiratory Growth, Related to Figure 3

(A) Images of Pab1-mCherry or Pub1-mCherry expressed at endogenous levels in WT cells. (Top) 6 h after switching from YPL to SL medium. (Bottom) 25 min after switching from SCD to SC medium (glucose deprivation). Scale bar = 1 μm.

(B) Images of Pbp1-yoEGFP (yeast optimized EGFP) in cells growing 3 h in SL medium and then treated with indicated concentrations of 1,6-hexanediol (1,6-HD) for 10 min. Scale bar = 1 μm.

(C) Images of Pbp1-GFP in cells growing in SL medium with DMSO or 25 μg/ml cycloheximide (CHX). Images were taken 1 h after switch. Note that CHX treatment did not change the distribution pattern of Pbp1. Scale bar = 1 μm.

A

```
low complexity regions: SEG 45 3.4 3.75
>Query

                                    1-328   MKGNFRKRDSSTNSRKGGNSDSNYTNGGVP
                                            NQNNSSMFYENPEITRNFDDRQDYLLANSI
                                            GSDVTVTVTSGVKYTGLLVSCNLESTNGID
                                            VVLRFPRVADSGVSDSVDDLAKTLGETLLI
                                            HGEDVAELELKNIDLSLDEKWENSKAQETT
                                            PARTNIEKERVNGESNEVTKFRTDVDISGS
                                            GREIKERKLEKWTPEEGAEHFDINKGKALE
                                            DDSASWDQFAVNEKKFGVKSTFDEHLYTTK
                                            INKDDPNYSKRLQEAERIAKEIESQGTSGN
                                            IHIAEDRGIIIDDSGLDEEDLYSGVDRRGD
                                            ELLAALKSNSKPNSNKGNRYVPPTLRQQ
phhmdpaiisssnsnsknenavstdtstpaa     329-507
agapegkppqktsknkkslsskeaqieelk
kfsekfkvpydipkdmlevlkrssstlksn
sslppkpisktpsaktvspttqisagkses
rrsgsnisqgqsstghttrsstslrrrnhg
 sffgaknphtndakrvlfgksfnmfiksk
                                    508-569 EAHDEKKKGDDASENMEPFFIEKPYFTAPT
                                            WLNTIEESYKTFFPDEDTAIQEAQTRFQQR
                                            QL
nsmgnavpgmnpamgmnmggmmgfpmggps      570-700
aspnpmmngfaagsmgmympfqpqpmfyhp
smpqmmpvmgsngaeegggnisphvpagfm
aagpgapmgafgypggipfqgmmgsgpsgm
                    pangsamhshg
                                    701-722 HSRNYHQTSHHGHHNSSTSGHK
```

B

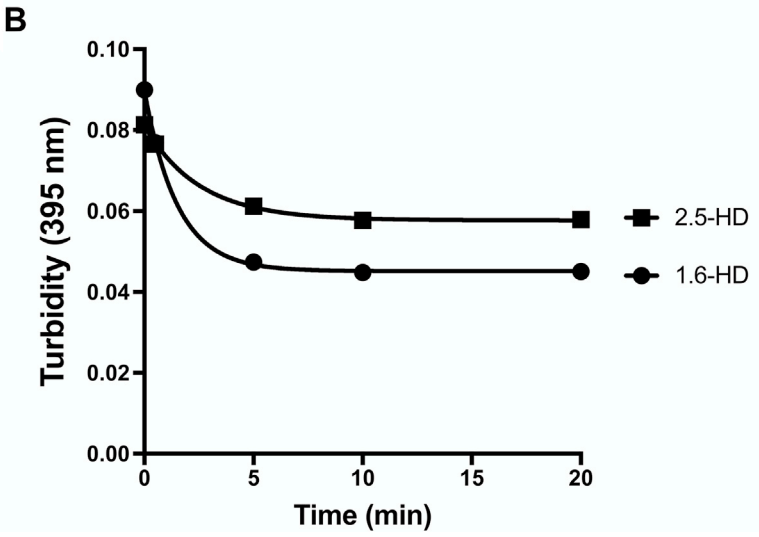

Figure S4. Low Complexity Regions within the Pbp1 Protein and Sensitivity of Pbp1_LC Fibrils to Hexanediols, Related to Figure 4

(A) Low complexity sequences identified using the SEG program. (Left column) low complexity region. (Right column) non-low complexity region.

(B) Dissolution of the Pbp1_LC fibrils by the 1,6- or 2,5-hexanediols (HD). Note that the fibrils were more sensitive to 1,6-HD. Data were mean ± SD from 3 independent experiments.

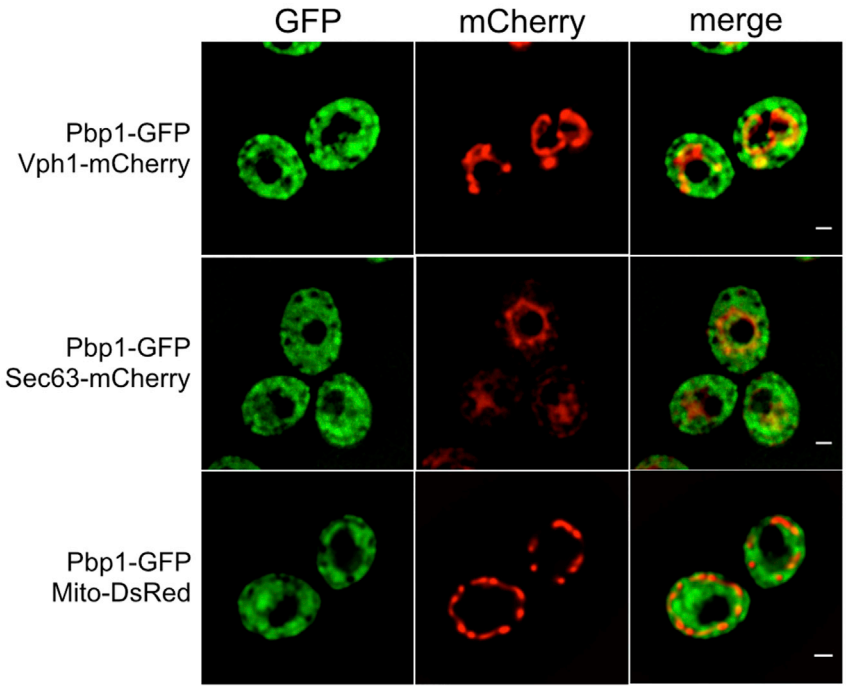

Figure S5. Localization of Pbp1 in Relation to Organelle Markers, Related to Figure 5

Images of cells expressing Pbp1-GFP with either Vph1-mCherry (vacuole), Sec63-mCherry (endoplasm reticulum), or Mito-DsRed (mitochondria) in SL medium. Note that the localization of Pbp1 is completely exclusive of mitochondria, suggesting it may form a condensate surrounding mitochondria. Scale bar = 1 μm.

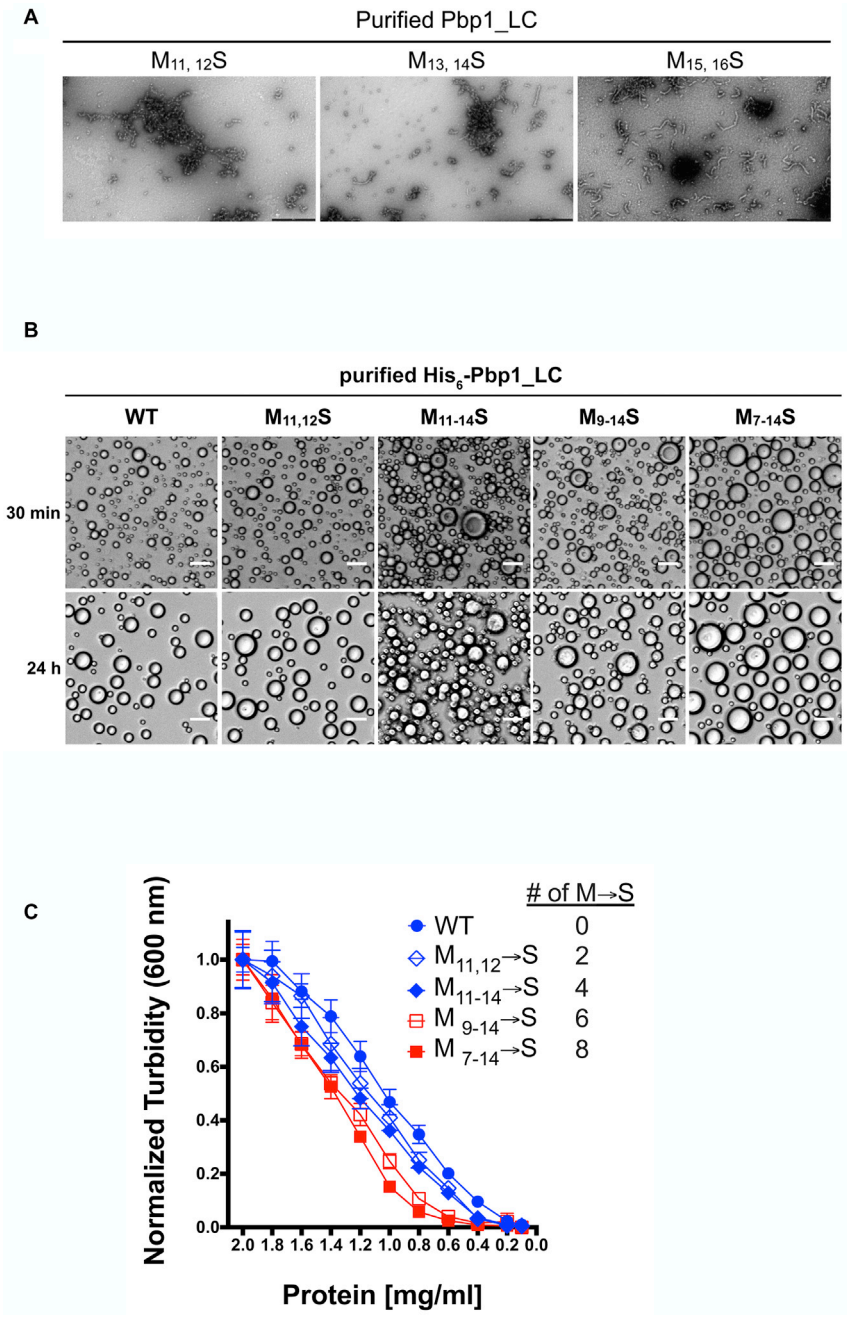

Figure S6. Properties of Fibrils or Phase-Separated Droplets Formed by the Indicated M → S Mutants within the LC Region of Pbp1, Related to Figure 6

(A) Electron micrographs of purified GFP-Pbp1_LC bearing indicated M to S mutations. All 3 Pbp1_LC variants showed reduced ability to form fibrils. $M_{11,12}S$ showed the weakest ability. Scale bar = 500 nm.

(B) Phase-separated droplet formation by purified His_6-Pbp1_LC containing indicated methionine to serine mutations. Images were taken 30 min and 24 h after lowering the salt concentration. Scale bar = 10 μm.

(C) Dissolution of phase-separated droplets formed from the indicated proteins by dilution. Turbidity was measured by light scattering at 600 nm. Phase-separated droplets formed by the variant bearing 8 methionine mutations dissolved more readily following dilution of the protein concentration. Data were mean ± SD from 3 independent experiments.

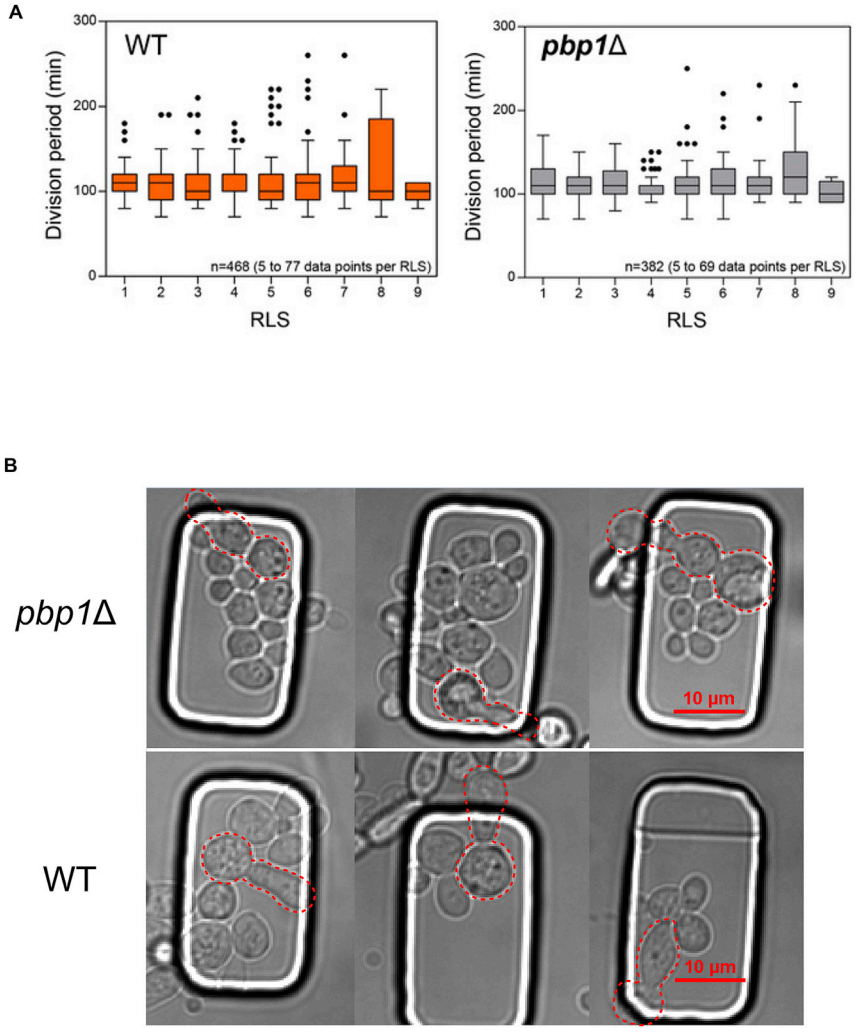

Figure S7. Microfluidic Imaging and Analysis of Cell Division for WT and *pbp1Δ* Cells in Glucose Medium, Related to Figure 7

(A) *pbp1Δ* cells exhibited comparable division times compared to WT in the presence of glucose. The division period was plotted against replicative lifespan (RLS) for WT and *pbp1Δ* cells. Each boxplot contains data from n = 5-77 and n = 5-69 for WT and *pbp1Δ* cells, respectively. In total, data from 468 (WT) and 382 (*pbp1Δ*) division events were recorded.

(B) Bright field images of representative WT and *pbp1Δ* cells with abnormal morphology at terminal stage.